![KIT logo](Karlsruhe Institute of Technology)

Investigation of field distribution in superconducting microwave resonators

Untersuchung der Feldverteilung in supraleitenden Mikrowellen-Resonatoren

Bachelor Thesis of

Markus Neuwirth

At the Department of Physics
Physikalisches Institut (PI)

Reviewer: Prof. Dr. Alexey Ustinov
Advisor: Dr. Martin Weides
Second advisor: Dr. Hannes Rotzinger

Duration:: 20. August 2012   –   14. March 2013

I declare that I have developed and written the enclosed thesis completely by myself, and have not used sources or means without declaration in the text.

Karlsruhe, DATE

. . . .
 (Markus Neuwirth)

Zusammenfassung

Eines der interessantesten Forschungsgebiete in der modernen Physik ist die kosmische Hintergrundstrahlung in der Astronomie. Extragalaktische hochenergetische Photonen kreuzen auf ihrem Weg zur Erde interstellare Materie, wie Gase und Staubwolken. Sie werden gestreut, absorbiert und die absorbierte Energie im tief infraroten Frequenzbereich reemittiert. Diese Photonen enthalten Information über die Emissionen kalter Objekte, wie Planeten, oder über weit entfernte Galaxien mittels Rotverschiebung. Anhand dieser Photonen kann man viel über die Entstehung von Sternen und Planeten lernen.

Des weiteren wird die kosmische Hintergrundstrahlung als Momentaufnahme des sehr jungen Universums betrachtet, welche Information über den Urknall, sowie dunkle Materie oder dunkle Energie liefern könnte. Mit 98% aller Photonen und 50% der beobachtbaren Luminosität bietet die kosmische Hintergrundstrahlung im infraroten Bereich ($0{,}1 - 10$ THz) großes Potenzial um den Kosmos besser zu verstehen [Bar09, Maz04].

Um diesen reichhaltigen Fundus an Phänomenen erforschen zu können, benötigt man sehr empfindliche Detektoren. Unter all diesen stechen die Supraleiter durch sehr wenig Rauschen heraus, da sie bei sehr niedrigen Temperaturen, meist unterhalb von 1 K, betrieben werden.

Viele dieser supraleitenden Detektoren, wie der *transition edge sensor* (TES) oder der *superconducting tunnel junction detector* sind jedoch meist sehr schwer in große Arrays zu intergrieren. Die größten Arrays aus TES bestehen aus nicht einmal 100 Pixeln, wobei über 1000 Pixel in der heutigen Forschung benötigt werden. Außerdem sind sie meist schwer auszulesen, da zusätzliche Strukturen dafür benötigt werden.

Eine Ausnahme stellt der *microwave kinetic inductance detector* (MKID) dar. Dieser verspricht nicht nur sehr hohe Sensitivität, lässt sich aber auch in große Arrays integrieren und einfach auslesen.

Trifft ein Photon auf einen MKID, bricht es ein Cooper Paar auf und ändert damit die Oberflächenimpedanz des Supraleiters, was gleichzeitig zu einer Änderung in der kinetischen Induktivität führt. Es ist möglich, durch Integrieren des Supraleiters in einen Schwingkreis, die eintreffenden Photonen direkt zu beobachten, da die Änderung der kinetischen Induktivität die Resonanzfrequenz des Schwingkreises beeinflusst. Praktisch verschiebt sich also der zur Resonanzfrequenz gehörige Dip im Transmissionsspektrum, wenn ein Photon auf den MKID trifft.

Diese Technik erlaubt es zudem mehrere MKIDs veschiedener Resonanzfrequenzen gleichzeitig auszulesen, indem man sie mit dem selben Transmissionssignal speist. Außerdem sind so keine zusätzlichen Auslesestrukturen erforderlich [Gao08, Maz04, Kai11].

Diese Arbeit beschäftigt sich mit supraleitenden Mikrowellen-Resonatoren, im Speziellen mit *coplanar waveguide resonators* aus Niobium (Nb). Im Mittelpunkt stehen dabei die Auswirkungen von Oxidation auf die Resonanzfrequenz. Oxidation ist ein allgemeines Problem sämtlicher metallischer Bauelemente. Gerade bei der Verwendung von Mikrowellen-Resonatoren als Photonendetektoren ist es essenziell die Auswirkungen von Oxidation auf die Resonanzfrequenz zu kennen.

Die Hauptschwerpunkte dieser Arbeit liegen in den Grundlagen der Supraleitung und der Schwingkreise, Simulationen zu den Auswirkungen von Oxidation auf die Resonanzfrequenz, der Fabrikation von Mikrowellen-Resonatoren und schließlich der Vermessung der Resonatoren hinsichtlich Transmission.

In Kapitel 3 wird die grundlegende Idee hinter dieser Arbeit und die daraus folgende Strategie genauer erläutert.

Contents

List of Figures

List of Tables

1. Introduction

One of the most interesting fields of research in physics today is that of the cosmic microwave background (CMB) radiation in astronomy. Extragalactic high energy photons travel through interstellar gases and dust clouds on their way to the Earth. They are scattered, absorbed and reemitted in the far-infrared range. Studying these photons gives information about emission from cold objects like planets or distant galaxies via light with red shift and therefore about star and planetary formation, which occurs deep in space.

The CMB radiation also is considered to be "a snapshot of the very infant universe" (p. 2, [Bar09]), which may provide further knowledge about the big bang and consequential dark matter and dark energy. With about 98% of all photons and 50% of the observable luminosity the CMB radiation in the far-infrared range ($0.1 - 10$ THz) contributes a lot to a better understanding of the cosmos better [Bar09, Maz04].

To explore this richness of phenomena it needs very high sensitive detectors. Among these superconductors stand out due to very little noise. They operate at very low temperature, mostly below 1 K, therefore they almost lack of thermal fluctuations.

There have been many superconducting detectors like the transition edge sensor (TES) or superconducting tunnel junction (STJ) detectors. They all provide very high sensitivity but it is very difficult to integrate them into large arrays. The largest arrays of TES contain less than 100 pixels, but more than 1000 pixels are required. For read out it needs extra structures like superconducting quantum interference devices (SQUID), which are superconducting rings involving Josephson junctions, this makes it even more difficult to create large arrays and fast data handling.

At this point the microwave kinetic inductance detectors (MKID) come into play. They provide very high sensitivity but are also easily integrable into large arrays and easy to read out.

Photons hitting the MKIDs break up Cooper pairs in the superconductor changing its surface impedance. This leads to a change in the kinetic inductance. Integrating the superconductor into a resonant circuit makes it possible to observe the photons, as a change in kinetic inductance also affects the resonance frequency. In the transmission spectrum of the resonator the amplitude and phase related to the resonance frequency of the resonator shift when a photon hits the resonator.

This passive way of reading out provides the opportunity of coupling several resonators with shiftet frequencies to the same transmission signal (called *frequency-domain multiplexing*) making it possible to read out several detectors at the same time, moreover additional read out structures are not required [Gao08, Maz04, Kai11].

This thesis deals with superconducting microwave resonators, particularly coplanar waveguide (CPW) resonators made of niobium (Nb). Especially the effect of oxidation on the resonator's resonance frequency is of interest. Oxidation is an everyday problem to all metallic structures and devices. Since the main usage of these superconducting microwave resonators is photon detection via frequency shift it is essential to know how oxidation affects the resonance frequency.

The main sections of this thesis are the basics of superconductivity and resonant circuits, simulations of the effect of oxidation on the resonance frequency, the fabrication of microwave resonators and finally the transmission measurement. In chapter 3 the basic idea and thus the strategy of this work is explained.

2. Theoretical background

This thesis deals with superconducting microwave resonators, their properties and measuring them in a microwave network setting. Therefore this first chapter is about the basic physics of superconductivity, the physics of parallel and series resonant circuits and their use for microwave resonators and lastly about microwave network analysis.

2.1. Basics of superconductivity

Superconductivity was discovered in 1911 when Kamerlingh Onnes studied the electrical resistivity of mercury. He observed that at a certain temperature, later to be called critical temperature T_c, around 4 K the resistivity dropped to zero. The fact that the resistance dropped instantly to zero and not gradually lead to the assumption that the mercury transformed into a novel state characterized by zero electrical resistance. This state was called superconductivity [Sch97].

2.1.1. Critical temperature

The critical temperature T_c depends on the material of the superconductor. For most metals T_c is below 10 K, for some alloys T_c can be slightly above 20 K, and for high temperature superconductors T_c can be up to 133 K [EH00].
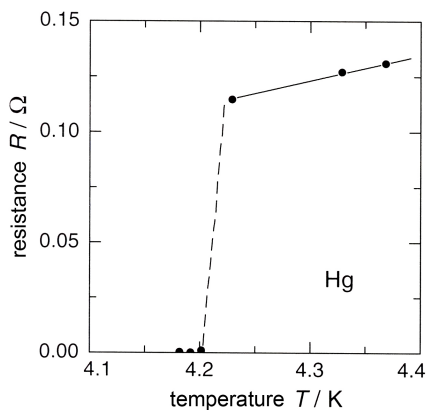
Figure 2.1 The electrical resistance of mercury as a function of the temperature T. At a certain temperature T_c, called *critical temperature*, the resistance drops to zero. Figure from [EH00].
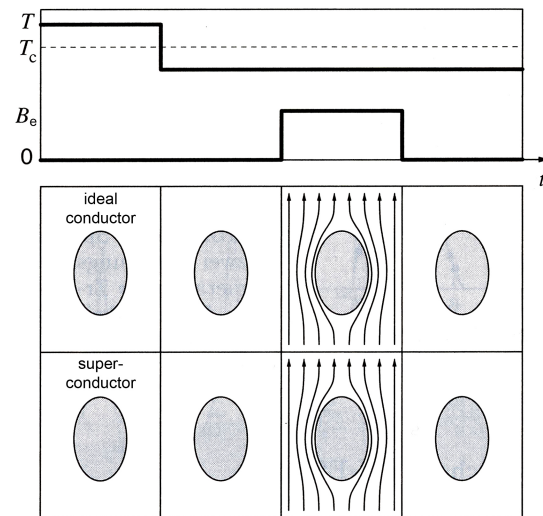
Figure 2.2 An ideal conductor and a superconductor in an external magnetic field. In the upper part of this figure one can see the time curves of the temperature T and of the external field B_e. In the lower part of the figure one can see two ellipsoidal conductors and the flow of the magnetic field. Here the external field is applied for temperatures below the critical temperature T_c, due to Lenz's law both conductors stay field-free during the whole experiment. Figure from [EH00].
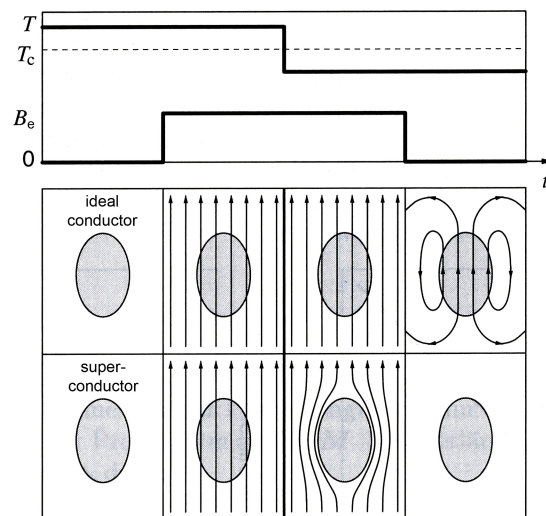
Figure 2.3 An ideal conductor and a superconductor in an external magnetic field. In the upper part of this figure one can see the time curves of the temperature T and of the external field B_e. In the lower part of the figure one can see two ellipsoidal conductors and the flow of the magnetic field. The external field is applied above the critical temperature T_c and therefore penetrates both conductors. By lowering the temperature below T_c the field gets suppressed out of the superconductor but it stays constant in the ideal conductor. After switching off the external field the ideal conductor preserves the internal field flow. Figure from [EH00].
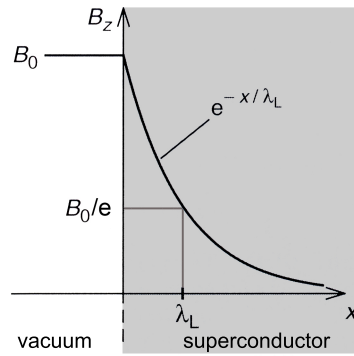
Figure 2.4 Behaviour of the magnetic field on the interface of a superconductor ($x > 0$). Inside the superconductor the field decreases exponentially. The London penetration depth is defined as the length where the field B_0 has decreased to B_0/e. Figure after [EH00].

2.1.2. The Meissner-Ochsenfeld effect

Until 1933 superconductors were considered to be simply ideal conductors with zero resistance. Then Meissner and Ochsenfeld discovered that superconductors also act like ideal diamagnets, thus the magnetic field inside the superconductor below T_c is always zero. The difference between an ideal conductor and a superconductor are shown in figures 2.2 and 2.3 and can be described as follows:

Take an ideal conductor below T_c and apply an external magnetic field. The magnetic field will not penetrate into the conductor, since according to Lenz's law there will always (zero resistance) be a induced current that generates a magnetic field in the opposite direction to that of the external field. The actual superconductor will act the same way.

Now take an ideal conductor and a superconductor above T_c and apply an external magnetic field. The magnetic field will penetrate the conductor and the superconductor completely. But when cooling both conductors below T_c the superconductor will suppress the magnetic field immediately whereas the ideal conductor will still be penetrated by the magnetic field. If you turn off the applied external field the ideal conductor will even create a current flow to preserve the magnetic field inside [EH00].

2.1.3. The London equations and penetration depth

In 1935 F. and H. London used the Maxwell equations to describe the behaviour of an ideal conductor and an ideal diamagnet at the same time. To derive these so called London equations one must use the electron's equation of motion

$$m\dot{\vec{v}} = -e\vec{E} - \frac{m\vec{v}}{\tau} \tag{2.1}$$

where m is the mass and $\vec{v}$ is the velocity of the electrons, $\vec{E}$ is the electrical field and τ is the mean free path. In an ideal conductor $\tau \to \infty$ which yields the current density, also often called the *first London equation*.

$$\frac{\mathrm{d}\vec{j}}{\mathrm{d}t} = \frac{n_\mathrm{s}e^2}{m}\vec{E} \tag{2.2}$$

where n_s is the density of superconducting charge carriers called Cooper pairs (see 2.1.4). Using the Maxwell equation $\mathrm{rot}\vec{E} = -\partial\vec{B}/\partial t$ we get

$$\frac{\partial}{\partial t}\left(\mathrm{rot}\vec{j} + \frac{n_\mathrm{s}e^2}{m}\vec{B}\right) = 0 \tag{2.3}$$
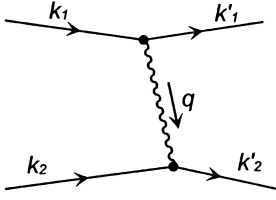
Figure 2.5 Diagram showing two electrons of wave vector $\vec{k}_1$ and $\vec{k}_2$ interacting with each other via a phonon of wave vector $\vec{q}$. Figure from [Sch97].

which reveals the magnetic flux to be steady. According to the Meissner effect not only $\partial\vec{B}/\partial t$ but $\vec{B}$ itself must vanish and we get

$$\mathrm{rot}\vec{j} = -\frac{n_\mathrm{s}e^2}{m}\vec{B} \tag{2.4}$$

which is called the *second London equation.*

Unlike in section 2.1.2 assumed, the magnetic field actually penetrates into the superconductor like in figure 2.4. The solution of this problem yields

$$B_\mathrm{z}(x) = B_0 e^{-x/\lambda_\mathrm{L}} \tag{2.5}$$

where λ_L is the *London penetration depth*

$$\lambda_\mathrm{L} = \sqrt{\frac{m}{\mu_0 n_\mathrm{s}e^2}}. \tag{2.6}$$

Since the density of superconducting charge carriers n_s is dependent on the temperature T, λ_L also depends on the temperature. Below T_c typical values of λ_L for bulk Niobium are around 30 nm whereas close to T_c $\lambda_\mathrm{L} \to \infty$ for $n_\mathrm{s} \to 0$. A more detailed consideration [EH00] yields the temperature dependence of λ_L

$$\lambda_\mathrm{L}(T) = \frac{\lambda_\mathrm{L}(0)}{\sqrt{1 - (T/T_\mathrm{c})^4}}. \tag{2.7}$$

2.1.4. Cooper pairs

In 1956 L. N. Cooper showed how two weakly interacting electrons have lower energies than the Fermi ground state. The interaction occurs via phonons. Imagine an electron moving through a lattice of positive ions interacting with them due to Coulomb interaction. This interaction bends the lattice for a certain time and creates a vibrational mode or a phonon, which itself interacts with another electron (see figure 2.5). One can consider the wave vector $\vec{k}_1$ of the first electron, the wave vector $\vec{k}_2$ of the second electron and the phonon $\vec{q}$. Conservation of momenta yields

$$\vec{k}_1 = \vec{k}'_1 + \vec{q} \tag{2.8}$$
$$\vec{k}'_2 = \vec{k}_2 - \vec{q} \tag{2.9}$$
$$\vec{k}_1 + \vec{k}_2 = \vec{k}'_1 + \vec{k}'_2. \tag{2.10}$$

Since both electrons lose energy during this process, the energy of the coupled electrons, called *Cooper pair*, is lower than the sum of the energies of both free electrons. The

difference of the Fermi ground state energy and the energy of one of the coupled electrons of a Cooper pair is called energy gap of the superconductor Δ. Therefore one must apply at least an amount of energy $E_{\min} = 2\Delta$ to excite the electrons and to split a Cooper pair. Electrons are fermions and therefore two interacting electrons cannot be in the same state which leads to the fact that the spins of the electrons are oppositely oriented and the total spin of a Cooper pair is zero. Cooper pairs are bosons and can occupy the same quantum mechanical state. The ground state of a superconductor is treated as a shared state of all Cooper pairs [EH00].

2.2. Superconducting microwave resonators
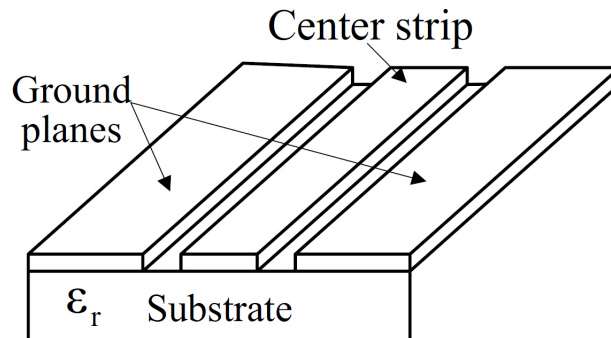
Figure 2.6 Geometry of coplanar waveguide. Center strip and ground planes consist of a metal, in this case superconductive niobium. The substrate is a dielectric, in this case silicon. The center strip is seperated from the ground planes via two gaps. Figure from [Gao08].

This thesis deals with Coplanar Waveguide (CPW) Resonators as shown in figure 2.6. To understand the physics of a CPW Resonator we first take a look at series and parallel RLC circuits, as a CPW Resonator near resonance always can be modeled by a equivalent RLC circuit. In the following sections we follow the textbook of D. M. Pozar [Poz05].

2.2.1. Series resonant circuits

Figure 2.7 shows a series resonant circuit consisting of a resistor R, an inductor L and a capacitor C. Since this is an oscillating circuit the ohmic resistance $R = \frac{U}{I}$ is replaced by the impedance $Z = \frac{U(t)}{I(t)}$ with its real and imaginary part

$$Z_{\text{in}} = R + iX = R + i\omega L - i\frac{1}{\omega C} \tag{2.11}$$

where R is the resistance, X is the reactance and ω is the frequency. This leads to a complex power that is delivered to the resonator
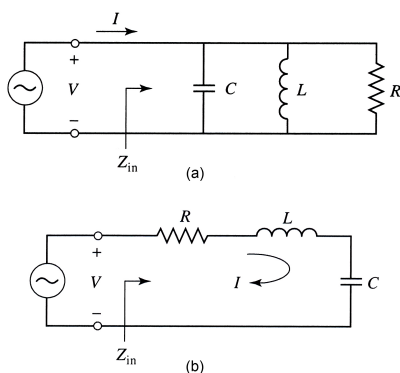
Figure 2.7 Parallel (a) and series (b) resonant circuit consisting of a resistance R, an inductivity L and a capacitance C. Figure from [Poz05].

$$P_{\text{in}} = \frac{1}{2}VI^* = \frac{1}{2}Z_{\text{in}}\,|I|^2$$
$$= \frac{1}{2}\,|I|^2 \cdot \left(R + i\omega L - i\frac{1}{\omega L}\right). \tag{2.12}$$

The power loss of the resonator is given by

$$P_{\text{loss}} = \frac{1}{2}\,|I|^2\,R, \tag{2.13}$$

the average magnetic energy stored in the resonator is

$$W_{\text{m}} = \frac{1}{4}\,|I|^2\,L \tag{2.14}$$

and the average electric energy stored in the resonator is given by

$$W_{\text{e}} = \frac{1}{4}\,|V_{\text{c}}|^2\,C = \frac{1}{4}\,|I|^2\,\frac{1}{\omega^2 C}, \tag{2.15}$$

where V_{c} is the voltage across the capacitor.
Resonance occurs when $W_{\text{m}} = W_{\text{e}}$, which leads along with equation 2.15 and equation 2.14 to the resonance frequency

$$\omega_0 = \frac{1}{\sqrt{LC}} \qquad f_0 = \frac{1}{2\pi}\omega_0 = \frac{1}{2\pi\sqrt{LC}}. \tag{2.16}$$

2.2.2. Parallel resonant circuits

The impedance of a parallel resonant circuit as shown in figure 2.7 is given by

$$Z_{\text{in}} = \left(\frac{1}{R} + \frac{1}{i\omega L} + i\omega C\right)^{-1} \tag{2.17}$$

and the complex power delivered to the resonator

$$P_{\text{in}} = \frac{1}{2}VI^* = \frac{1}{2}Z_{\text{in}}\,|I|^2 = \frac{1}{2}\,|I|^2\,\frac{1}{Z_{\text{in}}^*}$$
$$= \frac{1}{2}\,|V|^2 \cdot \left(\frac{1}{R} + \frac{i}{\omega L} - i\omega C\right). \tag{2.18}$$

The power loss of the resonator is

$$P_{\text{loss}} = \frac{1}{2}\frac{|V|^2}{R}, \tag{2.19}$$

the average magnetic energy stored in the resonator is

$$W_{\text{m}} = \frac{1}{4}\,|I_{\text{L}}|^2\,L = \frac{1}{4}\,|V|^2\,\frac{1}{\omega^2 L}, \tag{2.20}$$

where I_{L} is the current through the inductor, and the average electric energy stored in the resonator is

$$W_{\mathrm{e}} = \frac{1}{4} |V|^2 C. \tag{2.21}$$

$W_{\mathrm{m}} = W_{\mathrm{e}}$, equation 2.20 and equation 2.21 lead to the same resonance frequency

$$\omega_0 = \frac{1}{\sqrt{LC}} \qquad f_0 = \frac{1}{2\pi}\omega_0 = \frac{1}{2\pi\sqrt{LC}}. \tag{2.22}$$

The results for the parallel resonant circuit will be especially important throughout this thesis.

2.2.3. Quality factor and loss factor

Another important parameter is the quality factor or Q factor, which describes the loss of the resonator since it is inversely proportional to the dielectric loss tangent $tan\ \delta$

$$Q = \frac{1}{\tan\ \delta} \approx \frac{1}{\delta}, \tag{2.23}$$

where the approximation is only valid for $\delta \ll 1$. The quality factor is defined as

$$Q = \omega \cdot \frac{(\text{average energy stored})}{(\text{energy loss / second})} = \omega \cdot \frac{W_{\mathrm{m}} + W_{\mathrm{e}}}{P_{\mathrm{loss}}}. \tag{2.24}$$

At resonance ($W_{\mathrm{m}} = W_{\mathrm{e}}$) the quality factor is given by

$$Q = \begin{cases} \frac{1}{\omega_0 RC} & \text{for series resonator} \\ \omega_0 RC & \text{for parallel resonator.} \end{cases} \tag{2.25}$$

As the resonator is coupled to the feedline, the total loss is given by a coupling part and a intrinsic part. The corresponding Q is called "loaded Q" and therefore written as Q_{l}.

$$\delta_{\mathrm{l}} = \delta_{\mathrm{c}} + \delta_{\mathrm{i}} \quad \Rightarrow \quad \frac{1}{Q_{\mathrm{l}}} = \frac{1}{Q_{\mathrm{c}}} + \frac{1}{Q_{\mathrm{i}}} \tag{2.26}$$

Here Q_{i} (internal Q) represents the Q from above [Poz05].
For later usage it is important to know that the loss is additive:

$$\delta_{\mathrm{i}} = \sum_{\mathrm{j}} \delta_{\mathrm{j}} \tag{2.27}$$
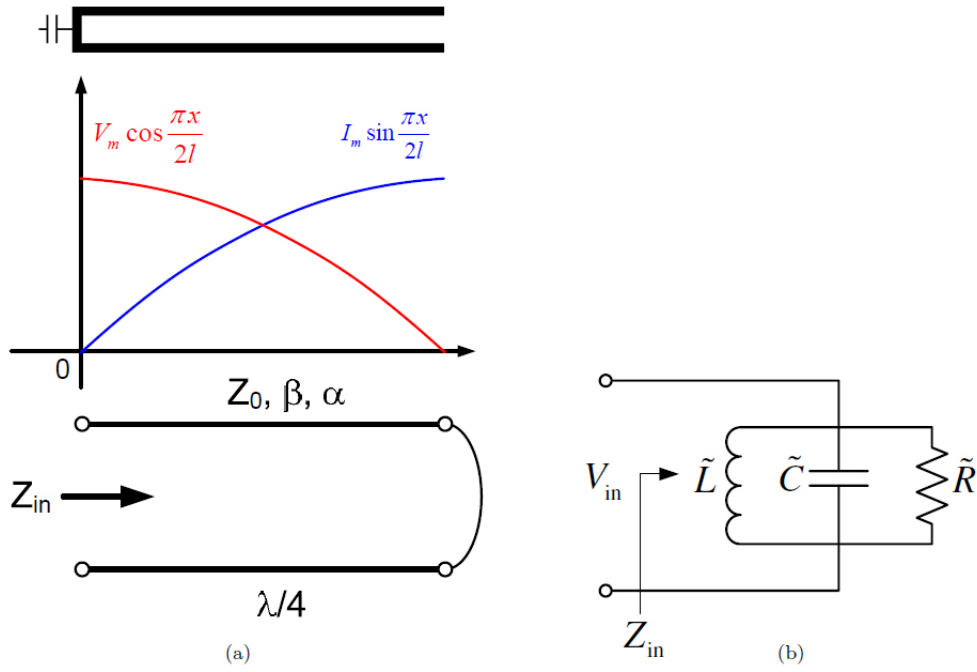
Figure 2.8 Illustration of a transmission line resonator and its equivalent RLC circuit. (a) shows a short-circuited $\lambda/4$ resonator and the corresponding standing wave patterns for voltage (red) and current (blue) distributions. (b) shows the equivalent RLC parallel resonance circuit. This approximation is only valid near the resonance frequency. Figure after [Gao08].

2.2.4. Lumped element and transmission line theory

As mentioned before the coplanar waveguide resonator near resonance can by modeled by an equivalent lumped RLC circuit. In this section we discuss the relation between the lumped RLC resonator and its counterparts in the transmission line theory.

The transmission line theory describes a distributed RLC element of length l as shown in figure 2.8. In our case l will be $\lambda/4$, where λ is the wavelength.

The input impedance of the short-circuited transmission line [Poz05] is

$$Z_{\text{in}} = Z_0 \tanh(\alpha + i\beta)l = Z_0 \frac{1 - i \tanh \alpha l \cot \beta l}{\tanh \alpha l - i \cot \beta l} \tag{2.28}$$

where

$$\gamma = \alpha + i\beta = \sqrt{(R + i\omega L)(i\omega C)} \tag{2.29}$$

is the complex propagation constant. Here R, L and C are the distributed resistance, inductance and capacitance of the transmission line resonator.

$$Z_0 = \sqrt{\frac{L}{C}} \tag{2.30}$$

is its characteristic impedance.

Considering a small loss ($\alpha l \ll 1$) close to the resonance frequency ($\omega = \omega_0 + \Delta\omega$), equation 2.28 reduces to

$$Z_{\text{in}} = \frac{Z_0}{\alpha l + i\pi\Delta\omega/2\omega_0}. \tag{2.31}$$

We notice that equation 2.17 reduces to the same form

$$Z_{\text{in}} = \frac{1}{1/\bar{R} + 2i\Delta\omega\bar{C}},$$

(2.32)

where $\bar{R}$, $\bar{L}$, $\bar{C}$ are the lumped elements of the transmission line resonator. Using the resonance frequency

$$\omega_0 = \frac{\pi}{2l\sqrt{LC}} \quad \text{or} \quad f_0 = \frac{1}{4l\sqrt{LC}}$$

(2.33)

and comparing 2.31 to 2.32 yields

$$\bar{R} = \frac{2}{l}\frac{L}{RC} \quad \bar{C} = \frac{l}{2}C \quad \bar{L} = \frac{8l}{\pi^2}L.$$

(2.34)

Again $\bar{R}$, $\bar{L}$, $\bar{C}$ are the lumped elements and R, L and C are the distributed elements of the transmission line resonator [Gao08].
It is important to notice that this is only valid for $l = \lambda/4$ at the case of resonance.

Figure 2.8 shows the standing-wave distributions along the transmission line at the case of resonance. Voltage and current are given by

$$V(x) = V_{\text{m}}\cos\left(\frac{\pi}{2l}x\right) \quad \text{and} \quad I(x) = I_{\text{m}}\sin\left(\frac{\pi}{2l}x\right)$$

(2.35)

where V_{m} and I_{m} are the peak voltage and current. Therefore the electric and magnetic energy is given by

$$W_{\text{e}} = \frac{1}{2}CV(x)^2 = \frac{1}{2}CV_{\text{m}}^2\cos^2\left(\frac{\pi}{2l}x\right)$$
$$W_{\text{m}} = \frac{1}{2}LI(x)^2 = \frac{1}{2}LI_{\text{m}}^2\cos^2\left(\frac{\pi}{2l}x\right)$$

(2.36)

Calculating the total electric and magnetic energy leads to the same results in 2.34:

$$W_{\text{e,tot}} = \frac{1}{2}C\int_0^l V(x)^2 = \frac{1}{2}C\int_0^l V_{\text{m}}^2\cos^2\left(\frac{\pi}{2l}x\right) \overset{!}{=} \frac{1}{2}\bar{C}V_{\text{m}}^2$$
$$W_{\text{m,tot}} = \frac{1}{2}L\int_0^l I(x)^2 = \frac{1}{2}L\int_0^l I_{\text{m}}^2\cos^2\left(\frac{\pi}{2l}x\right) \overset{!}{=} \frac{1}{2}\bar{L}I_{\text{m}}^2$$

(2.37)

2.2.5. Capacitance and inductance

The capacitance of the resonator can be calculated from equations 2.21 or 2.37 if the total stored energy of the resonator is known. A theoretical way of calculating the capacitance will be discussed in section 2.2.5.1.
The total inductance L of the resonator is separated into an external inductance L_{ext} and an internal inductance L_{int}. The external inductance is defined by the magnetic fields around the resonantor and its geometry and is therefore called "geometric inductance". The internal inductance is again separated in internal magnetic inductance L_{m} and kinetic inductance L_{kin}.

The kinetic inductance arises from the electrons in the conductor. External fields applied to the resonator force the electrons to move, which leads to a current flow that can be described by the Drude formula [Kit06, AM07]

$$\vec{J} = \left(\frac{nq^2\tau}{m} \right) \vec{E} \tag{2.38}$$

with the current density $\vec{J}$ and the applied electric field $\vec{E}$. The Drude conductivity is therefore given by

$$\sigma = \left(\frac{nq^2\tau}{m} \right) \tag{2.39}$$

where n is the density of charge carriers, q its charge, m its mass and τ its mean free time. This model describes electrons moving through a conductor and scattering after a certain time τ. The conductivity will turn complex for a time-dependant electric field with frequency ω:

$$\sigma(\omega) = \frac{\sigma_0}{1 + i\omega\tau} = \sigma' - i\sigma'' = \frac{ne^2\tau}{m + m\omega^2\tau^2} - i\frac{ne^2\omega\tau^2}{m + m\omega^2\tau^2} \tag{2.40}$$

This describes a delay in the response of the electrons to the external force caused by the applied electric field. In superconductors $\tau \to \infty$, therefore the imaginary part becomes noticeable and this can cause a significant kinetic inductance [Doy08].
Thus the total inductance is given by

$$L = L_{\text{ext}} + L_{\text{int}} = L_{\text{ext}} + L_{\text{m}} + L_{\text{kin}}. \tag{2.41}$$

where $L_{\text{ext}} = L_{\text{geo}}$.

2.2.5.1. Geometric capacitance and inductance

To calculate the geometric capacitance and inductance we follow J. Gao [Gao08]. Using conformal mapping technique and reducing the thickness of our CPW resonator to zero we get so called complete elliptic integrals of the first kind describing the height of the resonator:

$$K = K(k) = \int_0^1 \frac{1}{\sqrt{(1 - x^2)(1 - k^2 x^2)}} \, dx \tag{2.42}$$

$$K' = K(k') = \int_1^{1/k} \frac{1}{\sqrt{(x^2 - 1)(1 - k^2 x^2)}} \, dx \tag{2.43}$$

where $k = \frac{w}{w + 2g}$ and $k' = \sqrt{1 - k^2}$. w is the width of the center strip of the resonator and g is the width of the gap.
The capacitance and inductance can be expressed by

$$C = \epsilon_{\text{eff}} \epsilon_0 \frac{4K(k)}{K(k')} \tag{2.44}$$

$$L = L_{\text{geo}} = \mu_0 \frac{K(k')}{4K(k)} \tag{2.45}$$

and

$$\epsilon_{\text{eff}} = \frac{1 + \epsilon_{\text{r}}}{2} \tag{2.46}$$

where ϵ_{r} is the dielectric constant of the substrat beneath the conductor (for further details see [Gao08]).

2.2.5.2. Internal inductance

In the case of a thin conductor of thickness $t \approx 50\text{nm}$, accordingly between the limits of $t \ll \lambda_{\text{L}}$ and $t \gg \lambda_{\text{L}}$, the kinetic inductance L_{kin} depends on the thickness and on the London penetration depth. This is caused by $\sigma \propto \tau$ and τ is restricted by the thickness of the conductor. S. Doyle [Doy08] derived an appropriate formula to describe the internal inductance for this problem by taking all variations in current density over the entire cross-sectional area of the conductor into account:

$$L_{\text{kin}} = \frac{\mu_0 \lambda}{4w} \left[\coth\left(\frac{t}{2\lambda}\right) + \left(\frac{t}{2\lambda}\right) \text{cosec}^2 \left(\frac{t}{2\lambda}\right) \right] \tag{2.47}$$

$$L_{\text{m}} = \frac{\mu_0 \lambda}{4w} \left[\coth\left(\frac{t}{2\lambda}\right) - \left(\frac{t}{2\lambda}\right) \text{cosec}^2 \left(\frac{t}{2\lambda}\right) \right] \tag{2.48}$$

where λ is the London penetration depth, w the width of the conductor and t its thickness (for further details see [Doy08]).
This yields

$$L_{\text{int}} = L_{\text{m}} + L_{\text{kin}} = \frac{\mu_0 \lambda}{2w} \coth\left(\frac{t}{2\lambda}\right). \tag{2.49}$$

We notice that by changing the thickness of the conductor we change the internal inductance and thus the total inductance. According to equation 2.33 this will change the resonance frequency of the resonator.

2.3. Microwave network analysis

For measuring microwave signals we take a look at a N-port microwave network like shown in figure 2.9, whereas in between the ports may be any kind of transmission line [Poz05]. The terminal lines marked $t_1 \ldots t_{\text{N}}$ define the ports where the voltages and currents are tapped. V_{n}^+ and I_{n}^+ stand for the voltages and currents of the incident wave at port n, V_{n}^- and I_{n}^- stand for the voltages and currents of the reflected wave. The total voltage and current at the nth port is given by

$$V_{\text{n}} = V_{\text{n}}^+ + V_{\text{n}}^- \tag{2.50}$$

$$I_{\text{n}} = I_{\text{n}}^+ + I_{\text{n}}^-. \tag{2.51}$$
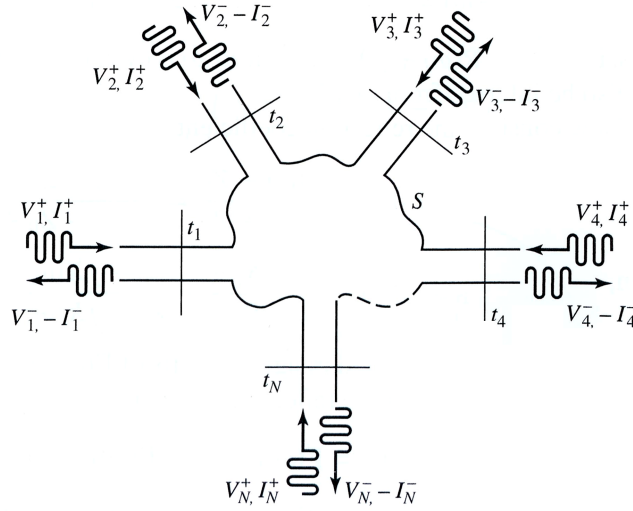
Figure 2.9 Sketch of arbitrary N-port microwave network. V^+ and I^+ stand for voltage and current of the incident wave at each port whereas V^- and I^- stand for voltage and current of the reflected wave at each port. $t_1 \ldots t_N$ stand for the ports where voltage and current are tapped. In between the ports may be any arbitrary structure or transmission line S. Figure from [Poz05].

In order to relate all voltages and currents in the microwave network one uses the impedance matrix $[Z]$:

$$
\begin{pmatrix} V_1 \\ V_2 \\ \vdots \\ V_N \end{pmatrix} = \begin{pmatrix} Z_{11} & Z_{12} & \ldots & Z_{1N} \\ Z_{21} & & & \vdots \\ \vdots & & & \vdots \\ Z_{N1} & \ldots & \ldots & Z_{NN} \end{pmatrix} \begin{pmatrix} I_1 \\ I_2 \\ \vdots \\ I_N \end{pmatrix}, \tag{2.52}
$$

which can be written in matrix form as

$$
[V] = [Z][I]. \tag{2.53}
$$

Similar to the impedance matrix the admittance matrix $[Y] = [Z]^{-1}$ is defined:

$$
\begin{pmatrix} I_1 \\ I_2 \\ \vdots \\ I_N \end{pmatrix} = \begin{pmatrix} Y_{11} & Y_{12} & \ldots & Y_{1N} \\ Y_{21} & & & \vdots \\ \vdots & & & \vdots \\ Y_{N1} & \ldots & \ldots & Y_{NN} \end{pmatrix} \begin{pmatrix} V_1 \\ V_2 \\ \vdots \\ V_N \end{pmatrix}, \tag{2.54}
$$

or in matrix form

$$
[I] = [Y][V]. \tag{2.55}
$$

Measuring the total voltages or currents at each port is not a straightforward task. A way more practical way of measuring microwave signals is to measure transmission from one port to another or reflection at the ports. Therefore one needs a connection between V_n^- and V_n^+. This is described by the scattering matrix $[S]$:

$$
\begin{pmatrix} V_1^- \\ V_2^- \\ \vdots \\ V_N^- \end{pmatrix} = \begin{pmatrix} S_{11} & S_{12} & \dots & S_{1N} \\ S_{21} & & & \vdots \\ \vdots & & & \vdots \\ S_{N1} & \dots & \dots & S_{NN} \end{pmatrix} \begin{pmatrix} V_1^+ \\ V_2^+ \\ \vdots \\ V_N^+ \end{pmatrix},
\tag{2.56}
$$

or in matrix form

$$
[V^-] = [S][V^+].
\tag{2.57}
$$

Each element of the scattering matrix stands for either a reflection at a port or a transmission from one port to another. One specific element is determined as

$$
S_{ij} = \left. \frac{V_i^-}{V_j^+} \right|_{V_k^+ = 0 \text{ for } k \neq j}.
\tag{2.58}
$$

For the actual measurement a 2-port network analyser is used. In a 2-port network the scattering matrix simplifies to

$$
\begin{pmatrix} V_1^- \\ V_2^- \end{pmatrix} = \begin{pmatrix} S_{11} & S_{12} \\ S_{21} & S_{22} \end{pmatrix} \begin{pmatrix} V_1^+ \\ V_2^+ \end{pmatrix},
\tag{2.59}
$$

where S_{11} stands for the reflection at port 1, S_{22} the reflection at port 2, S_{12} the transmission from port 2 to port 1 and S_{21} the transmission from port 1 to port 2. For a better overview this is listed in table 2.1.

Table 2.1 Physical meaning of the elements of a 2×2 scattering matrix characterizing a 2-port microwave network.

matrix element	physical meaning
S_{11}	reflection at port 1
S_{12}	transmission from port 2 to port 1
S_{21}	transmission from port 1 to port 2
S_{22}	reflection at port 2

3. Idea and chip design

This thesis deals with the effect of oxidation on the resonance frequency of superconducting microwave resonators. The material of interest is niobium (Nb).

The basic idea is to manufacture Nb resonators and to specifically oxidize them afterwards. A silicon wafer with Nb on top is used for manufacturing. In figure 3.1 the whole chip design is shown. The chip is 5×5 mm in size and contains 10 microwave resonators. The resonators are capacitively coupled to a feedline, which is connected to microwave cables via bond pads and bond wire at the large areas at each end of the feedline. All five resonators on one side of the feedline have the same length and therefore the same resonance frequency. The ones on the top half are weakly coupled, that means they have a short coupling element next to the feedline, the ones below the feedline are strongly coupled. Due to the shorter coupling element the ones at the top side are shorter than the ones below and therefore have a higher resonance frequency. A shorter coupling element also leads to a higher Q-factor. The structures in between the resonators are test structures and of no interest for this work. The plus symbols to the right of each resonator are for aligning the mask to the wafer for later anodization (see chapter 5.4). The connection area and the two different coupling elements can be seen in more detail in figure 3.2, this figure shows both the design and the manufactured chip.

Since there are resonators with two different resonance frequencies on the chip two dips are expected in the transmission spectrum. The dips do not necessarily have to be sharp, that is a small bandwidth, since there might be variances in the fabrication process for every resonator. Even a slight variance in the etch depth might shift the frequency. But for later experiments this is acceptable.

After the fabrication the resonators are specifically oxidized via anodic oxidation, or *anodization*. Two resonators at a time, one of each kind, are anodized for the same amount of time and voltage resulting in an oxide layer with a certain thickness. The first pair is left unoxidized as a reference. In the end there are 5 pairs of resonators with different oxide layers on top resulting in 10 different resonance frequencies. In summary this process turns two dips in the transmission spectrum into ten dips with a certain distance to each other. The frequency shift due to oxidation is of interest, as it corresponds to a reduced film thickness and increased dielectric surface contribution.

In order to obtain accurate results the resonance frequencies and the shifts should be approximately known when first designing the resonators. Therefore simulations of the resonators with and without oxide layers are done. For the details on the simulations see chapter 4. In chapter 5 the fabrication process and in chapter 6 the final measurements are described.
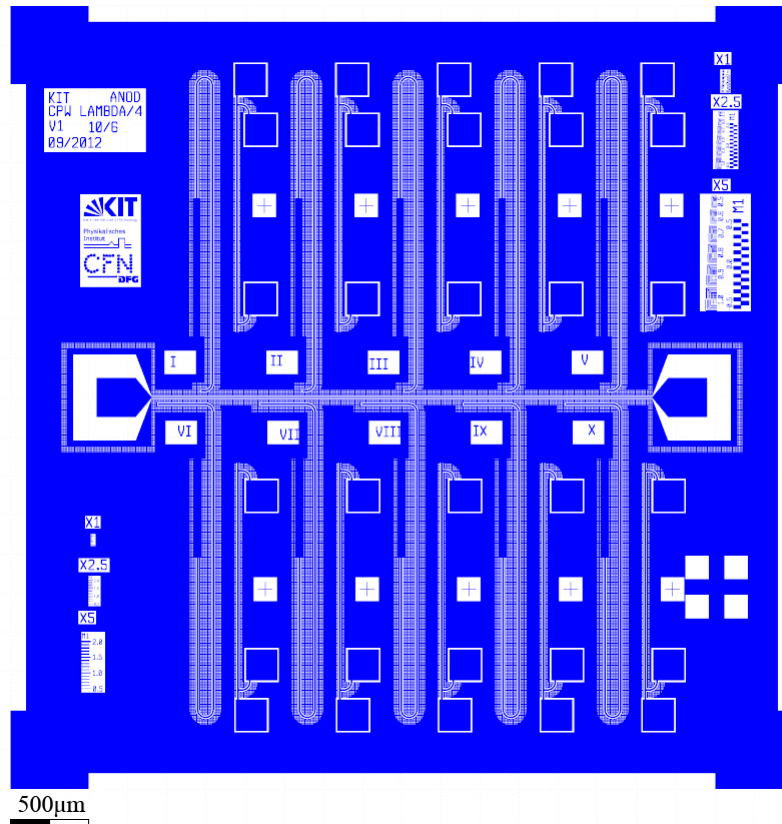
Figure 3.1 Overview of the total chip design. The blue color symbolizes the Nb layer whereas the white areas are to be etched thus symbolize the gaps. There are 10 resonators on the chip. Resonators I to V have the same length and a small coupling element, resonators VI to X are slightly longer than the upper ones since they have a longer coupling element. In between the resonators are several test structurs. The plus symbols are for aligning the mask to the right position during the anodization process (see chapter 5.4). The small dots all around the structures are flux traps, which trap any magnetic flux that may penetrate the superconducting material.
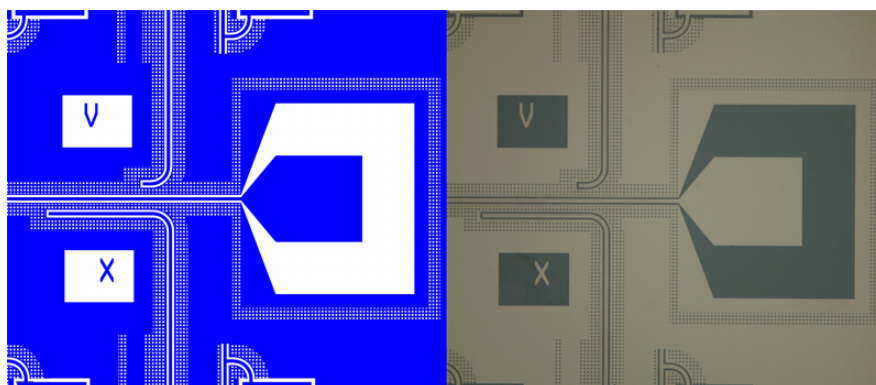
Figure 3.2 The design (left) and the manufactured chip (right) in detailed view of the connection area and the two different coupling elements of the resonators. The small dots all around the structures are flux traps, which trap any magnetic flux that may penetrate the superconducting material.

4. Simulations

This chapter deals with two different simulations of coplanar waveguide resonators. The major focus of these simulations lies on the influence of oxidation of niobium on the resonance frequency and the quality factor of the resonators.

The first section describes the simulation of the resonators' cross section with focus on the capacitance and inductance changes and thereof resonance frequency and Q-factor. For these simulations a free software called FEMM was used.

The second section deals with the simulation of two different resonators from the chip with Sonnet. These simulations focus on design optimization for fabrication.

The full details on the simulation's results can be found in appendix C.

4.1. Cross section simulation using FEMM

FEMM stands for Finite Element Method Magnetics. It is used to simulate and solve "low frequency electromagnetic problems on two-dimensional planar and axisymmetric domains [...] linear/nonlinear magnetostatic problems, linear/nonlinear time harmonic magnetic problems, linear electrostatic problems, and steady-state heat flow problems" (p. 6, [Mee10]). The Simulations for this thesis were made with FEMM version 4.2.

FEMM can be controlled via graphical user interface or Lua scripting. Lua is a C based programming language. The Lua script programmed during this work can be found in appendix A [Mee10].

The simulated CPW resonator has a conductor width of 10 μm, a gap width of 6 μm and a thickness of 100 nm for the first simulation, later a thickness of 50 nm. The calculations in FEMM are made for a depth of the cross section of 1 μm, for the calculation of the total energies and consequential capacitance and so on a total length of the resonator of $l = 14.698$ mm was used. Above the resonator there's vacuum or air with a relative permittivity of $\epsilon_\mathrm{r} = 1$ and the substrate is of silicon with an $\epsilon_\mathrm{r} = 12$.

In figure 4.1 one can see the whole simulated cross section area. For different regions different mesh sizes were used to reduce computation time. The regions in the middle next to the actual resonator have the finest meshsize. For further details see appendix A. A general meshsize parameter ms was defined to control the meshsize easily.

In tabular 4.1 one can see a comparison between calculated specific capacitance of a CPW resonator via FEMM and analytical via elliptic integrals (see appendix B.1) as described in 2.2.5.1. The results calculated via FEMM differ from the analytical results and surprisingly decrease for smaller ms, thus finer meshsize. Although the variance is very small for

all ms, higher ms should be used. But for ms > 5 the meshsize is larger than the structures itself. Therefore ms = 5 was used for further simulations.

Since the values slightly differ from analytically calculated values the results might not be exact and are not supposed to be considered as such. But within the frame of this work they are sufficient and are considered as guidelines for fabrication and what's to be expected during the experiment and measurement.

Table 4.1 Comparison between specific capacitance cacultated via FEMM and analytical (see chapter 2.2.5.1.) One can see that for a higher meshsize parameter ms (which leads to larger meshsize) the variation between the results decreases.

	FEMM		analytical	
ms	E (J/μm)	C (F/μm)	C (F/μm)	variation (%)
5	$8.50091 \cdot 10^{-17}$	$1.70018 \cdot 10^{-16}$	$1.70757 \cdot 10^{-16}$	0.433
3	$8.48739 \cdot 10^{-17}$	$1.69748 \cdot 10^{-16}$	$1.70757 \cdot 10^{-16}$	0.591
2	$8.48221 \cdot 10^{-17}$	$1.69644 \cdot 10^{-16}$	$1.70757 \cdot 10^{-16}$	0.652
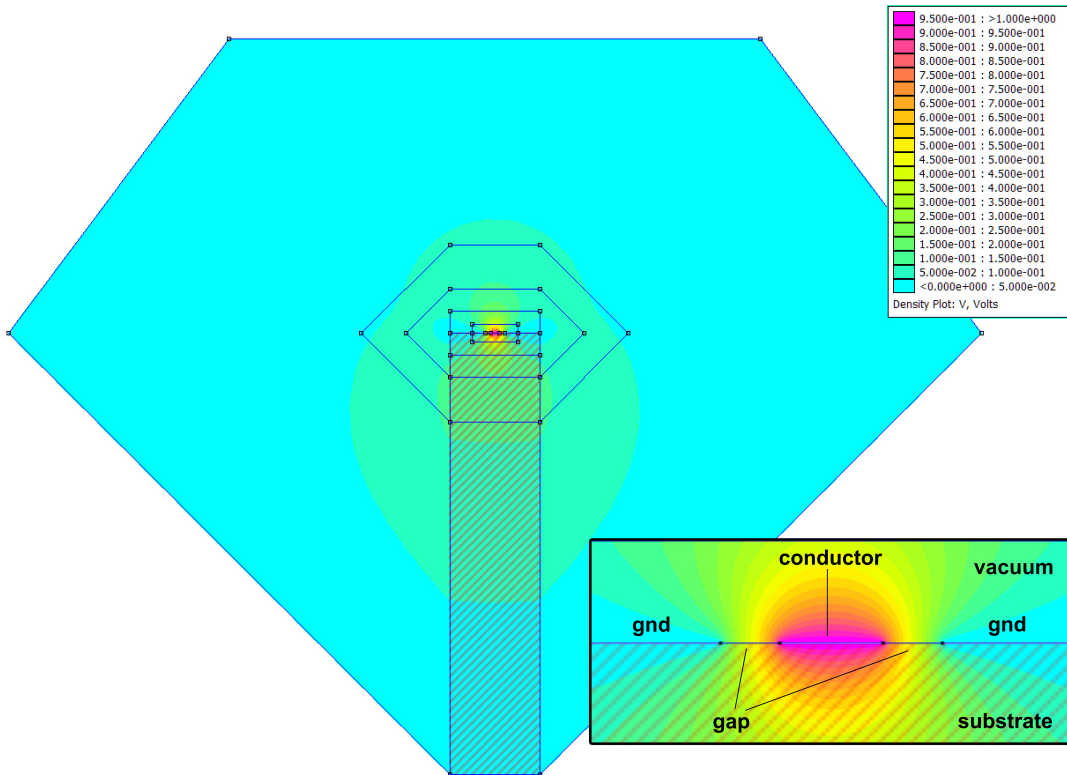
Figure 4.1 Voltage density plot of the CPW resonator's cross section created with FEMM, where the applied voltage on the conductor is 1V and on the ground 0V. The geometry used is 10 μm for the conductor's width, 6 μm for the gap width and 0.1 μm for the height of the conductor. More details of the setting's dimensions can be abstracted from appendix A, whereas in this figure the width of the oxide is 0 nm. The geometry of the exterior borders was chosen to be as large as possible and at the same time minimum processor-intensive.

From now on the conductor and ground plane thickness is set to be 50 nm, since the Nb layer's thickness of the wafers to be used for fabrication is 50 nm.

4.1.1. Oxide layer in the gap of the CPW resonator

A thin oxide layer with relative permittivity of $\epsilon_r = 35$ is put on the Nb. First due to simplification it is assumed that the oxide layer is formed only in the gap of the resonator next to the edge of the Nb layer like shown in figure 4.2 (b). Also it is assumed that the oxide is formed without consuming the Nb layer decreasing its thickness.

For oxide layer thicknesses from 0 nm to 150 nm in steps of 25 nm the total stored energy in the resonator is calculated by FEMM. The capacitance is caculated knowing the total energy but the inductance cannot be calculated this way, therefore the analytical value for L is used (see appendix B.1). This leads to an inductance of $L = 6.232$ nH.

The results in energy, capacitance and resonance frequency are listed in table 4.2. This simulation leads to a very small change in total energy for different oxide layer thicknesses thus only small changes in capacitance and resonance frequency. The change in energy and capacitance is only 1.406% leading to a change in resonance frequency of only 0.696%, which is an absolute change of 55.759 MHz. This can hardly be measured in an experiment considering process variations.

It is noticed that a change in the value of C affects the resonance frequency less than a change in the value of L would do, which leads to the assumption that a closer look at the inductance is needed.

Table 4.2 Total stored energy, capacitance and resonance frequency of CPW resonator for oxide layer with thickness t_{oxide} formed only in the gap without decreasing Nb layer thickness.

t_{oxide} (nm)	E (pJ)	C (pF)	f_0 (GHz)
0	1.249	2.499	8.013
25	1.252	2.504	8.006
50	1.256	2.512	7.993
75	1.259	2.517	7.984
100	1.261	2.523	7.975
125	1.265	2.530	7.965
150	1.267	2.534	7.958

4.1.2. Oxide layer all around the Nb layer decreasing its thickness

The results of section 4.1.1 led to a more detailed simulation of the resonators cross section. This time the oxide layer is put all around the Nb layer. Furthermore it also consumes the Nb layer decreasing its thickness, which according to section 2.2.5.2 effects on the inductance of the resonator. Therefore a bigger change in resonance frequency is expected. Again the relative permittivity of the oxide is $\epsilon_r = 35$.

In figure 4.2 (c) and (d) the gap of the resonator including oxide layers of 50nm (c) and 100nm (d) is shown. Kroger, Smith and Jillie state that during anodization, which is forced anodic oxidation (see section 5.4) about 0.9 nm are consumed for every 2.3 nm of NbO_x [KSJ81]. Herewith the remaining Nb layer thickness is calculated. The total inductance is calculated with equations 2.41 and 2.49 where λ is set to be 90 nm.

In table 4.3 the results of this simulation are listed. As the oxide layer decreases the Nb layer thickness, the maximum oxide layer thickness is set to be 125 nm. Here only about 1 nm of Nb is left. This leads to an extreme change in L and f_0. Therefore the values for oxide thickness of 125 nm are not representative. However, it does show that the thickness reduction of the Nb layer is the main reason for the change in resonance frequency.
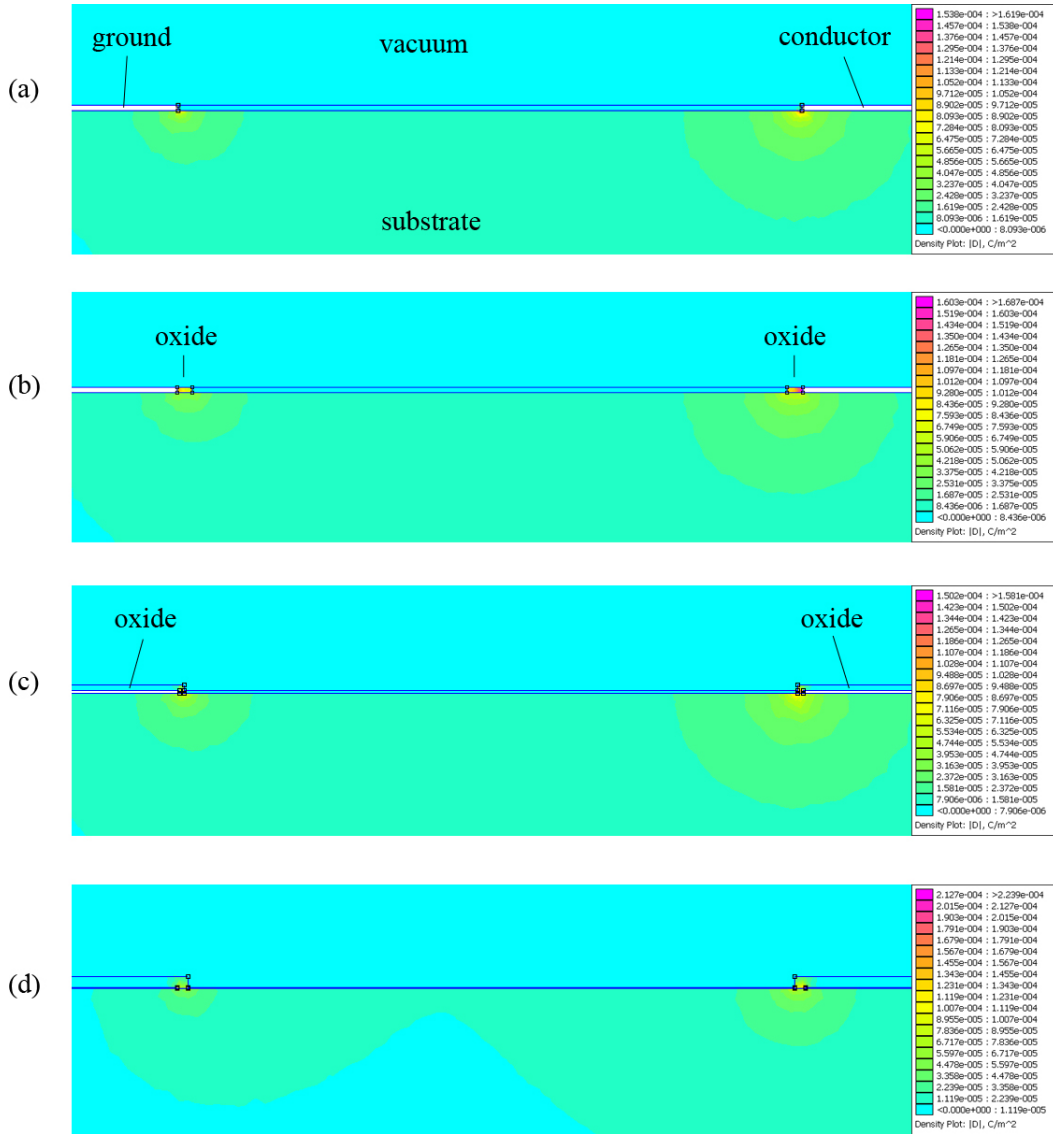
Figure 4.2 Flux density plot of one of the two gaps of the CPW resonator. On the left side is the left ground plane and on the right side is the conductor. The gap's width is 6 μm and the thickness of conductor and ground plane is 50 nm. (a) shows the setting without a oxide layer, in (b) the oxide layer is only formed in the gap next to the edge of the Nb layer without consuming it and decreasing its size. (c) shows an oxide layer all over the Nb layer with thickness of 50 nm, here about 30.4 nm of the Nb layer is left due to consumption by the oxide. In (d) the oxide layer is 100 nm thick leading to a remaining Nb layer of 10.8 nm. The flux density (zero for bluish color) indicates the losses in the resonator system. For comparison to the whole cross section see figure C.1.

Up to 100nm oxide thickness there is a change in total energy and capacitance of 1.040% and in inductance of 16.382%. The chance in resonance frequency is 7.783%, which is an absolute change of 609.486 MHz. This setting is much more realistic and leads to good results since a frequency shift of 600 MHz is definitely noticeable in the experiment.

Table 4.3 Total stored energy, capacitance, inductance and resonance frequency of CPW resonator for an oxide layer with thickness t_{NbO_x} formed all around the Nb layer and decreasing its thickness t_{Nb}. For $t_{NbO_x} = 125$ nm there is almost no Nb left, which leads to extreme changes in total inductance and resonance frequency.

t_{NbO_x} (nm)	t_{Nb} (nm)	E (pJ)	C (pF)	L (nH)	f_0 (GHz)
0	50.00	1.247	2.494	6.539	7.831
25	40.22	1.251	2.501	6.610	7.777
50	30.43	1.253	2.507	6.728	7.700
75	20.65	1.257	2.514	6.960	7.560
100	10.87	1.260	2.520	7.610	7.221
125	1.09	1.255	2.511	19.996	4.463

By changing the oxide layer the losses of the resonator change as seen in figure 4.2. This leads to a change in the quality factor of the resonator.

The different losses are set to be $\delta_{sub} = 1 \cdot 10^{-6}$ for the loss in the Si substrate, $\delta_{ox} = 1 \cdot 10^{-3}$ for the loss on the oxide layer interface and $\delta_{vac} = 0$ for the loss in vacuum. Together with the capacitance c of the substrate, the oxide layer and vacuum resulting of the specific energies stored in those layers the internal loss is given by

$$\delta_i = \frac{\delta_{sub}c_{sub} \cdot \delta_{ox}c_{ox} \cdot \delta_{vac}c_{vac}}{C_{tot}}, \tag{4.1}$$

where C_{tot} is the total capacitance of the system caculated of the total stored energy.

In table 4.4 the results for internal loss and quality factor are listed. The specific capacitance of the oxide layer changes the most since its relative volume change is the biggest. The substrate changes its specific capacitance despite the fact that its volume stays the same. This is caused by the change of the total capacitance due to the change of the conductor's thickness.

The internal quality factor Q_i is reduced with increasing oxide layer thickness. This was expected since the oxide layer deteriorates the overall quality of the resonator. Also this improves the visibility of the dip of the resonance in the transmission spectrum since it's getting broader.

Table 4.4 Capacitances c for the various layers and resulting internal loss δ_i and quality factor Q_i of the resonator system for increasing oxide layer thickness and decreasing Nb layer thickness. Here *vac* stands for vacuum, *sub* stands for substrate and *ox* stands for oxide layer.

t_{NbO_x} (nm)	t_{Nb} (nm)	c_{vac} (pF)	c_{sub} (pF)	c_{ox} (fF)	δ_i (10^{-6})	Q_i (10^6)
0	50.00	0.201	2.293	–	1.000	1.000
25	40.22	0.203	2.297	2.339	1.934	0.517
50	30.43	0.204	2.299	4.307	2.716	0.368
75	20.65	0.205	2.302	6.563	3.608	0.277
100	10.87	0.206	2.304	9.496	4.765	0.210
125	1.09	0.206	2.304	15.254	7.076	0.141

In figure 3.1 the whole chip design including 10 resonators is shown. According to the results of this simulation the 5 pairs of resonators will be anodized resulting in oxide layer thicknesses of 0, 25, 50, 75 and 100 nm.

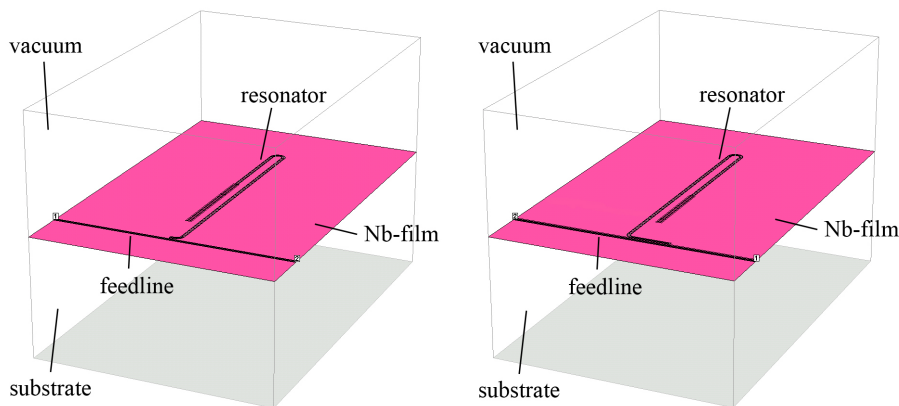## 4.2. Resonator design simulation using Sonnet

Figure 4.3 3D view of resonator simulation box in Sonnet. The weakly coupled resonator is on the left side and the strong coupled resonator is on the right side. The box is 2000×3000 μm in size, vacuum ($\epsilon_r = 1$) and substrate ($\epsilon_r = 12$) are 1000 μm thick.

Sonnet is a simulation software used to analyse 3D planar electromagnetic problems. 3D planar means the circuit geometry is 2D planar but layer on top of it and underneath it are three dimensional. Also the circuit geometry can contain several planar layers on top of each other [Son11].

This simulation is used to analyse the two different resonator designs on the chip (see figure 3.1). This yields information on where to find the dips according to which resonance frequency in the actual transmission measurement and whether to change the design of the chip for better results. It is important for the outcome of this work that the two resonator frequencies are remote from each other so they do not overlap when shifted by anodization.

The two resonators were cut out of the chip design and put into a box, see figure 4.3. The vacuum of $\epsilon_r = 1$ and the substrate of $\epsilon_r = 12$ are 1000 μm thick. The box is 2000×3000 μm in size. A transmission measurement was simulated and the resonance frequency was read out. To calculate the Q factor the -3dB method was used. The results are listed in table 4.5.

The difference between the two resonance frequencies is about 1.5 GHz. According to the results of the cross section simulation in section 4.1.2 the maximal shift of frequency is about 600 MHz, thus the resonator designs are suitable for this work.

The Q factor especially of the short resonator is extremely high leading to a very sharp dip, which is not easy to find in the spectrum. But in reality this may differ since there are other structures on the chip next to the resonators, like the test structures in between the resonators, the ceramic ground plane, to which the chip is attached and also the metallic box, containing the chip. In general the coupling gets bigger thus the Q gets smaller. Both resonance dips of the simulation are about -55 dB deep.

Table 4.5 Resonance frequency and Q factor of the weakly coupled (short) and strong coupled (long) resonators calculated by Sonnet.

	f_0 (GHz)	Q_l
short	10.164	508200
long	8.584	52340

4.2.1. Kinetic inductance check
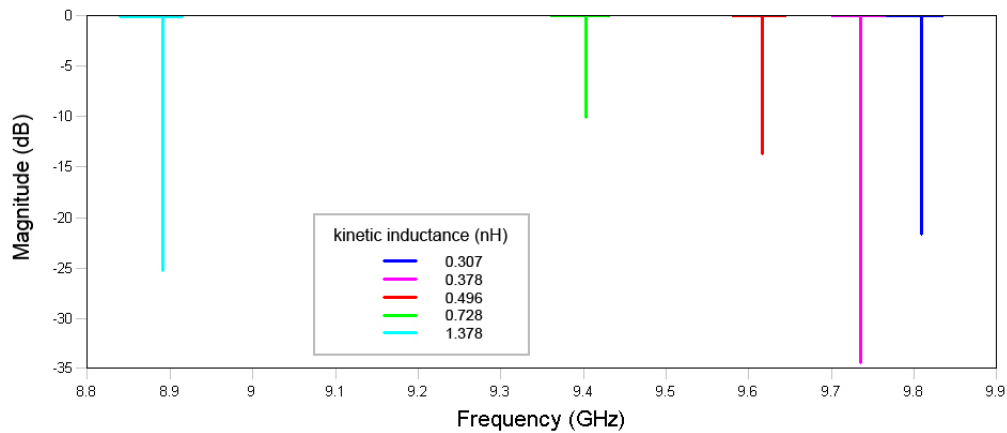
Figure 4.4 Resonance frequency dips in the transmission simulation of Sonnet. This simulation was made with the weakly coupled resonator. The five dips belong to different kinetic inductance values (listed in table C.4). The kinetic inductance increases from the right to the left side.

Sonnet also provides the option of changing the kinetic inductance of the metal. Another simulation was made using the values of kinetic inductance calculated during the simulations in section 4.1.2 to check how much the frequencies of the resonators on the actual chip will shift. The values of the kinetic inductance can be found in table C.4.

It is important to notice, that in the previous simulation no kinetic inductance was assumed, therefore even the resonance frequency of the resonator without an oxide layer will be changed by now, since there is a kinetic inductance for zero oxide thickness. It is also important to know, that Sonnet changes the kinetic inductance of the whole metal part in the box, even the feedline, therefore the frequency shifts might be different from the results in section 4.1.2. The results are listed in table 4.6.

The total change in resonance frequency is 9.352% which is an absolute change of 917.3 MHz. This shift is even bigger than the shift calculated in section 4.1.2.

Table 4.6 Resonance frequency of the weakly coupled (short) resonator for several kinetic inductance values according to the oxide layer thickness of section 4.1.2 calculated by Sonnet. It is important to notice that there is no actual oxide layer in the simulation with Sonnet.

t_{oxide} (nm)	L_{kin} (nH)	f_0 (GHz)
0	0.307	9.809
25	0.378	9.735
50	0.496	9.617
75	0.728	9.404
100	1.378	8.891

5. Fabrication

The fabrication process of the chip containing the resonators consists of several work stages with different tasks, shown in figure 5.1. In summary photolithography is used to create the structures on the substrate. First photoresist is applied on the substrate via spin coating, then it is exposed by UV light, where the chemical composition of the photoresist is modified. After developing the exposed part of the photoresist is removed from the substrate. Then the structures are created by chemical plasma etching.
The several steps are discussed in more detail in the following sections.

5.1. Spin coating

For the following applications there needs to be a uniform thin photoresist film on the substrate. To achieve this spin coating is used. First the photoresist is applied on the substrate, covering at least 60% of it. While spin coating the substrate is rotated at certain speeds to spread the photoresist by centrifugal force. The thickness of the resist decreases with increasing rotations per minute. This varies for different photoresist types. For this application Microposit S 1805 G2 photoresist was used. In figure 5.2 the thickness and its dependance on the spin speed is shown.

The photoresist manufacturer states that the maximum coating uniformity is typically attained between spin speeds of 3500 and 5500 rpm [Roh06]. But figure 5.2 shows that the thickness of the S 1805 does not vary to much with spin speed and the substrate used measures only 20 x 20mm. In this fabrication process a spin speed of 1000 rpm was used and this led to very good results. For detailed information of the spin coating parameters see appendix D. After spin coating the substrate is baked on a hotplate to consolidate the photoresist film.

5.2. Mask aligning and exposure

The process of mask aligning is to ensure that all structures are placed on the their designated position on the substrate while exposure, thus to manually align the mask, which is a negative of the structures, to the substrate. The instrument that was used in this fabrication process is the SUSS mask aligner MA6. It has a build in lamp for exposure.

There are three different modes of optical lithography, contact, proximity and projection lithography.

27

photoresist	Applying photoresist on the substrate via spin coating.
Nb-Layer	
substrate	

mask — Maskaligning and exposure.

Developing to remove exposed photoresist.

Creating structures via etching.

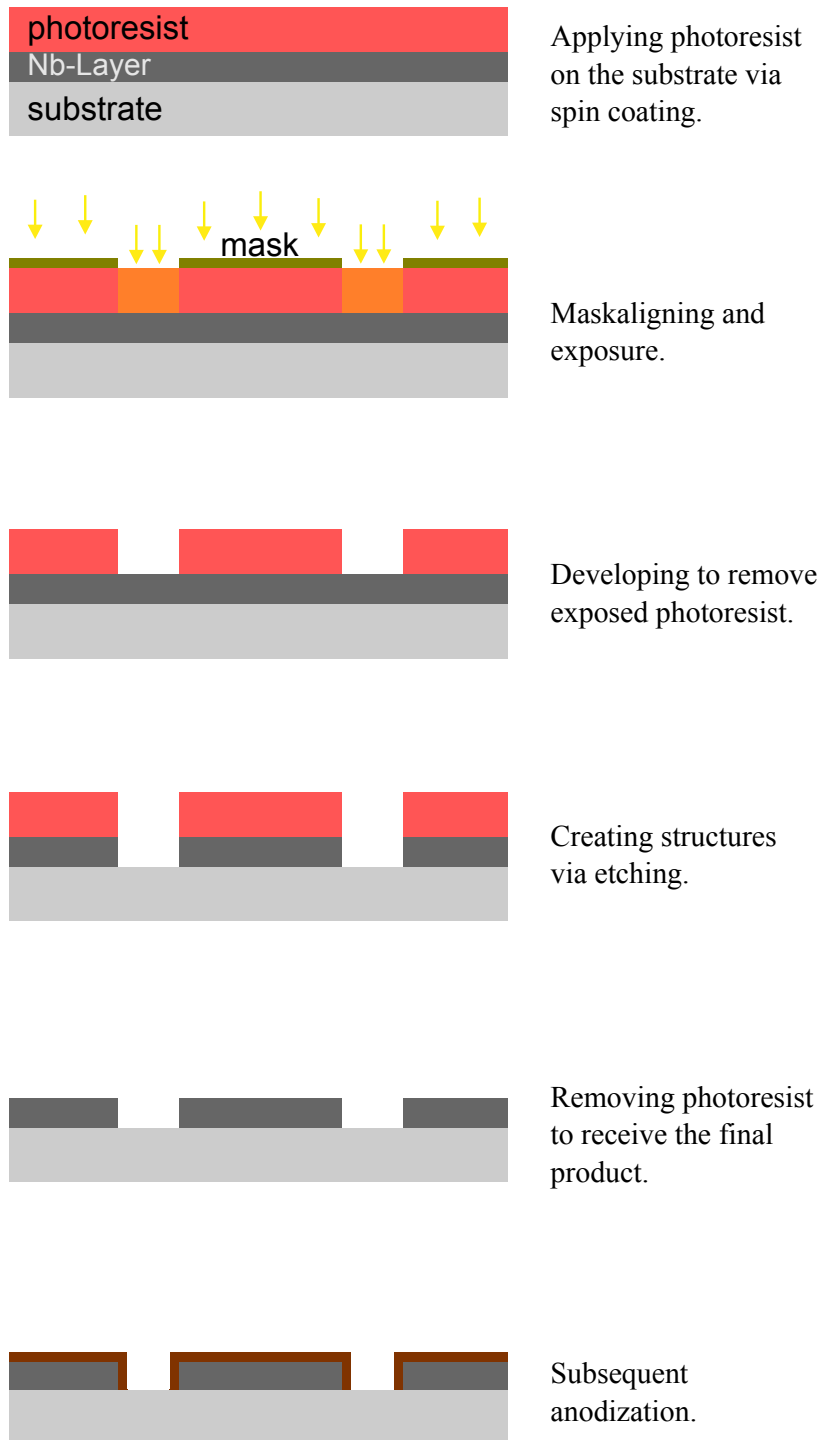Removing photoresist to receive the final product.

Subsequent anodization.

Figure 5.1 Schematic view of the whole fabrication process. Here a optical lithography process is shown using positive photoresist. The first five steps are done within the cleanroom. The final product is the structure of the coplanar waveguide resonator. Afterwards there is the anodization, which does not take place in the cleanroom.
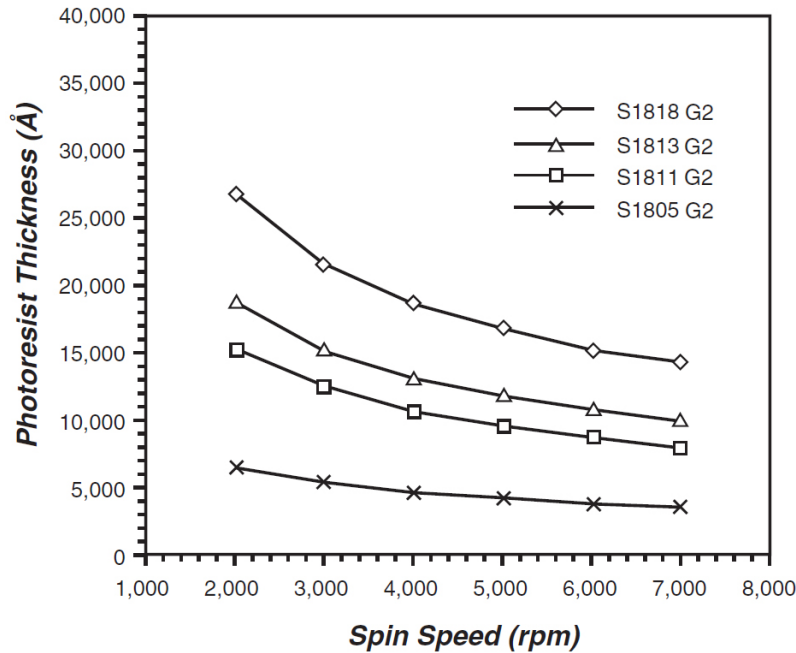
Figure 5.2 The thickness of Microposit S 1800 G2 photoresist versus the spin speed of the spin coater. The thickness of the resist decreases with the increasing square root of the spin speed. Figure from [Roh06].

When using contact lithography the mask is being pressed to the substrate to get the best resolution. To measure the resolution a parameter called minimum feature size (MFS) is used. It describes the size of the smallest structures that can be created on the substrate. For contact lithography $MFS = \sqrt{d \cdot \lambda}$, where d is the thickness of the photoresist and λ is the wavelength of the light used for exposure. A disadvantage of the contact mode is that the mask can be damaged. To avoid this the proximity mode can be used, where there is a small gap between the mask and the substrate. Therefore the resolution is lower for $MFS = \sqrt{(d+g) \cdot \lambda}$, where g is the thickness of the gap.

Using projection lithography avoids damaging the mask as in contact mode and it provides a better resolution than proximity lithography. The mask is not in contact with the substrate but an image of the mask is projected to the substrate. Theory of optics and interference yields a resolution of $MFS = k_1 \cdot \frac{\lambda}{NA}$, where k_1 is a technology constant, which takes everything non optical like lens errors and resist quality into account, and NA is the numerical aperture of the system [Was03].

For this work the hard contact mode of the SUSS MA6 was used.

During exposure the structure of the photoresist, which is a polymer, is modified. In general there are two types of photoresist, positive and negative resist. In positive resists the photons break the bonds of the polymer, which makes it less stable so it can easily be removed by the developer. In negative resist the photons link the polymers together. Here the unexposed resist is removed by the developer. This is illustrated in figure 5.3. The quality of the resist also effects on the resolution of the lithography process, this is termed contrast. As shown in figure 5.3 resists with high contrast lead to a steeper slope than resists with low contrast and therefore to a better resolution [Was03].

In general the exposure time and intensity must be exactly known. By exposing too long or too intense there is the risk of modifying too much photoresist, which also leads to a lower resolution. The same problem occurs in developing. Developing too long might remove too much resist and details in the structures might be gone. Figure 5.4 shows a comparison between the desgin and the manufactured resonators' bending at the top.
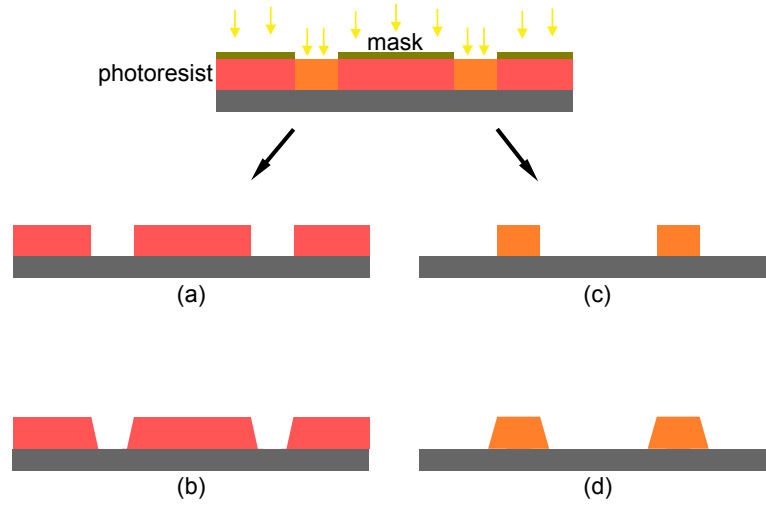
Figure 5.3 Schematic view of positive and negative photoresist. In positive resists (a, b) the photons break the bonds of the polymer so that it can easily be removed by a developer. In negative resists (c, d) the photons link the polymers together and therefore the unexposed parts of the resist are removed by the developer. This view also shows the difference between high and low contrast of photoresists. (a) shows an positive photoresist with high contrast producing very steep slopes whereas (b) shows an positive resist with low contrast producing wide slopes. (c) and (d) show the same for negative photoresist.

Here the smallest structures were not created properly, this might be caused by too much exposure or too long developing.

The resist used in this work is an positive photoresist with high contrast. The developer used is the Microposit MF-319, which is recomended for developing the S 1800 photoresists [Shi]. For an overall look at all specifications of the maskaligning, exposure and developing process see appendix D.

Figure 5.4 The design (left) and the manufactured chip (right) in detailed view of the bending area at the top of the resonators. The small dots all around the structures are flux traps, which trap any magnetic flux that may penetrate the superconducting material. Here the smallest of these flux traps were not created, which might be caused by too much exposure or too long developing. But for the experiment this detail is irrelevant.

5.3. Etching

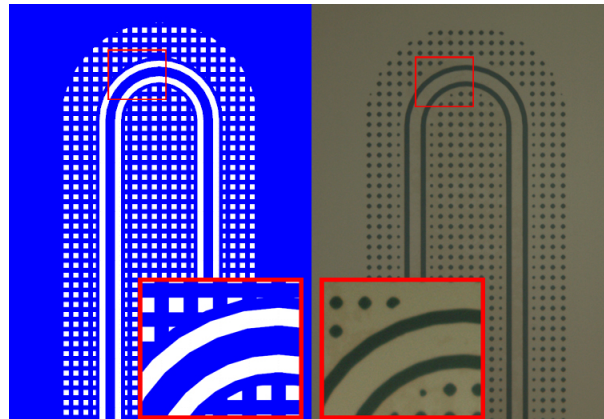Etching is a technique for material removal, in this case to create the gap between the center strip of the resonator and the ground plane surrounding it.
In general there are two types of etching, physical etching and chemical etching. Physical etching or sputtering relies on the momentum of particles hitting the wafer and knock out atoms at the surface, whereas chemical etching relies on reactions modifying the surface making it solutable or volatile. Further etch processes can be seperated into wet etching and dry etching [Was03].

Wet etching is a purely chemical process, using certain solutions to react with the wafer's surface. Wet etching consists of three steps. First the reactive species in the solution have to move to the surface, then a reaction must take place creating soluble etch products and finally the etch products have to move away from the surface.
The advantage of this procedure is that there are several recipes to etch mostly every material and also the surface is getting removed without damaging or modifying it like in physical etching. But the disadvantages are that the concentration of the etch solution needs to be very accurately controlled to get constant and reproducible etch rates. Often a great quantity of chemicals is consumed during a wet etching process. Also a large number of recipes are toxic, therefore the waste disposal is a problem. Another major drawback of wet etching is that structures with feature size smaller than one micron cannot be created well controlled [Was03].

Dry etching involves ionised gases, called plasma, produced in low pressure discharges. It is separated into plasma etching, where the material to be etched is in direct contact with the plasma, and ion beam etching (IBE), where the plasma is generated in a separate chamber and then is accelerated onto the material. To accelerate the ions voltage is applied on a grid in front of the plasma source. Mostly gases used for plasma creation are inert gases.
Also it is seperated into sputter etching (physical etching), where the ions knock of atoms on the surface, and chemical dry etching, where the surface atoms and the ionised gases form volatile etch products.
If using reactive gases containing fluorine, chlorine, bromine or oxygen instead of inert gases we speak of reactive ion etching (RIE), which was used in this fabrication process. Therefore this is treated seperately in section 5.3.1.
The advantage of dry etching in comparison to wet etching is that no chemical solution is needed and it is much more selective, thus more precise [Was03].

A general problem with etching is underetching, where the material is removed right beneath the resist layer, therefore the structures get bigger than intended. This occurs in both dry and wet etching. Furthermore the resist might be removed or deformed at its edges which also affects the structure's form and size. This is called resist peeling and mainly occurs in chemical etch processes. Both effects are illustrated in figure 5.5 [KR12].

5.3.1. Reactive ion etching

Reactive ion etching (RIE) is the most common etching technique. It is a mixture of chemical and physical etching, providing a much more selective, controllable and faster etch process than pure chemical or physical etching. The wafer is loaded into the plasma chamber where reactive gases containing fluorine, chlorine, bromine or oxygen are used. In this work's process SF_6 was used.
The plasma is generated by a voltage applied between two electrodes. The gas molecules
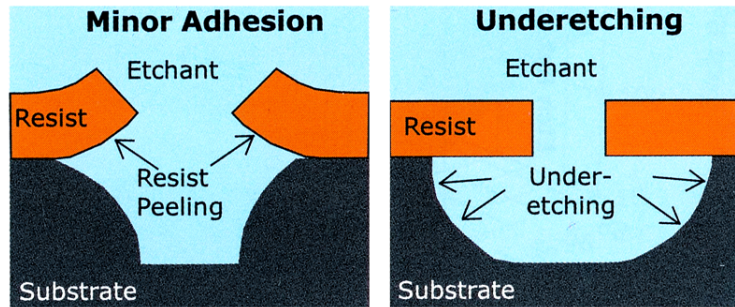
Figure 5.5 Illustration of underetching and resist peeling during etch processes. In the left image the photoresist layer is deformed and partially detached by the etchant which affects the resist's form and size. This is called resist peeling. In the right image the material gets removed by the etchant not only beneath the resist gap, where it is intended, but also beneath the resist itself. This is called underetching. Figure from [KR12].

are accelerated and collisions take place forming the plasma containing positive and negative ions as well as electrons, radicals and neutrals. This is called glow-discharge and takes place at very low pressure, typically about $10^{-3} - 0.1$ mbar.

Further collisions create more particles in the plasma like electrons knocking out other electrons from molecules or atoms. Also electrons can split molecules into radicals. In a SF_6 plasma total breakups of the original SF_6 molecules can be found as well as reactions like $e^- + SF_6 = SF_4 + F^+ + F^*$ (F^* stands for excited F, which is a radical) or $e^- + SF_6 = SF_4 + F2^{(R)}$ (where (R) symbolizes an excited Rydberg state) take place [BTB87]. But at the same time collisions take place where particles are lost as electrons and ionised molecules may recombine or several ions form molecules again. Also diffusion to the electrodes or through the walls of the chamber takes place. Therefore only a small fraction of the atoms and gas molecules in the plasma are ionised. Typically there is only about one charged atom per $1000 - 10^6$ neutral atoms. This makes $10^9 - 10^{12}$ ions per cm^3 [Oeh86, Eph81, Was03].

For the actual etching process the electrode on the wafer's side is negatively charged to shield the electrons, as they have a smaller mass and therefore receive greater kinetic energies from collisions than the ions. This leads to a bombardement of positive charged ions, which knock out atoms at the wafer's surface. At the same time chemical reactions between neutrals and the surface's atoms take place forming volatile etch products. This combination of sputtering and chemical etching provides a greater etch rate in vertical direction than in lateral direction, which leads to better etching results and steeper slopes. Therefore one can fabricate smaller structures on the wafer [Oeh86, Eph81].

5.4. Anodic oxidation

Anodic oxidation or anodization is a process used to oxidize metals, in this case a Nb film. In figure 5.7 the setup used for this work is shown. By applying voltage to the metal and the gold plate, in this case a copper plate, an electrical current occurs through the elctrolyte, which surrounds the Nb and the copper. Here the Nb film serves as the anode and the copper plate serves as the cathode. Electrons move to the cathode and oxygen ions move to the anode forming the oxide on the metal surface [dS07], here Nb_2O_5 [Wei06]. The electrolyte used for this work consists of 156 g ammonium pentaborate, 1120 ml ethylene glycol and 760 ml H_2O [KSJ81, Wei06].

As to be seen in figure 5.7 the contacts to the Nb and copper plate are made outside of the electrolyte. The Nb film is covered with photoresist revealing only an area of a pair of resonators, one weakly coupled and one strong coupled resonator. In this process about 0.9 nm are consumed and 2.3 nm of NbO_x are produced for each volt applied on the Nb
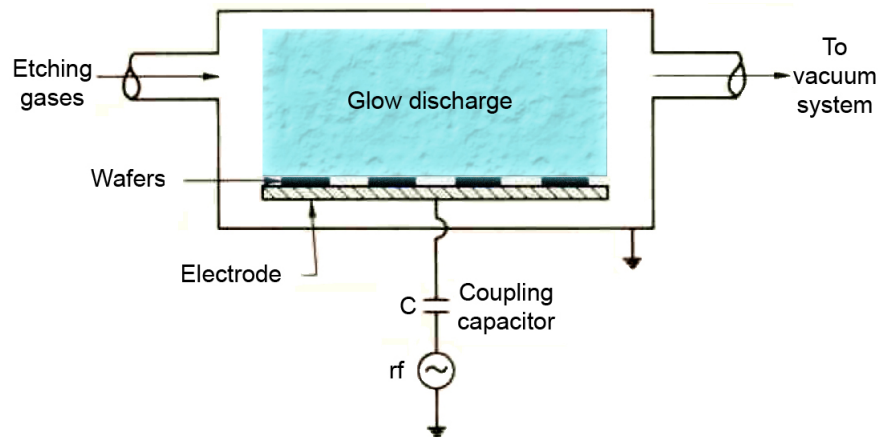
Figure 5.6 Sketch of a plasma reactor with one electrode where a voltage is applied via a coupling capacitor. *rf* stands for radio frequency, commonly frequencies at 13.56 MHz are used [Oeh86]. Due to the applied voltage the etching gases are accelerated and collide creating the plasma in a glow-discharge. Figure after [Oeh86].

and copper [KSJ81].

In the progress of this work only Nb samples were anodized to test the setup. The idea was to anodize pairs of resonators to shift their resonance frequency, but since the resonance dips could not be observed in the actual measurement (see chapter 6) the anodic oxidation of the resonators was abandoned.
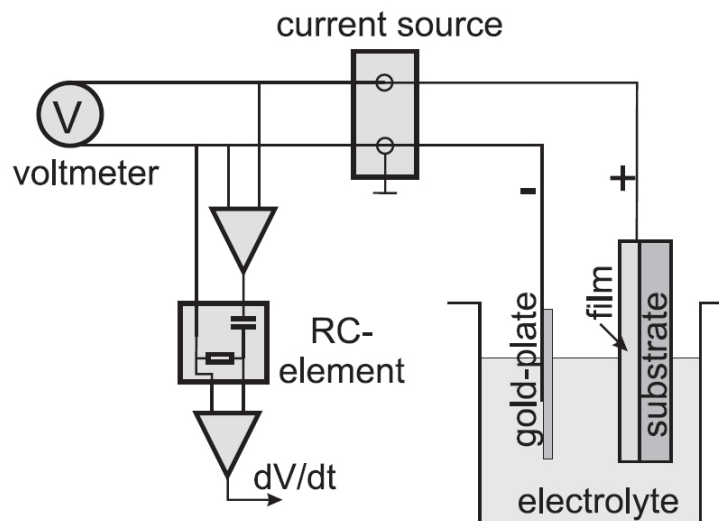
Figure 5.7 Sketch of the anodic oxidation setup. Instead of the gold plate a copper plate was used. The RC-element can be used to observe changes in the applied voltage for a detailed monitoring of the metal thickness. This was not used thus is not interesting for this work. Figure from [Wei06].

6. Measurements

This chapter deals with the transmission measurement of microwave resonators. For theory on this topic see section 2.3.

In summary there are 2 different samples made. At first there is the measurement of the designed chip without anodization, which failed at 4.2 K. There were several improvements on the setup done, which lead to no result. That is why a second measurement was made with another chip.

In section 6.1 the used setup is described. In section 6.2 the measurement and fitting process is described and finally in section 6.3 the results of the measurement are shown.

6.1. Setup

The measurements take place in liquid helium (^{4}He) at 4.2 K. A helium dewar and a dipstick is used. The box containing the chip is attached to the end of the dipstick making it possible to put it down to the ground of the helium dewar. The 2-port vector network analyzer (VNA) is connected to the feedline via coaxial cables to the dipstick, copper cables through the dipstick and finally stainless steel cables to the chip. To suppress reflexions at connectors there are attenuators with in summary 40 dB damping before and 3 dB damping behind the chip. The whole bottom part of the dipstick is enclosed inside a mu-metal shield to suppress the earths magnetic field inside the box. The dipstick with and without mu-metal shield is shown in figue 6.1.

To avoid thermal conduction from the copper cables to the chip there are so called DC blocks put between the copper and the stainless steel cables. This is done because of the failing of the first measurement, which led to the assumption of not being cold enough to see the resonators in the transmission spectrum (see section 6.3.1).

To get to lower temperatures the helium dewar is connected to a pump to decrease the pressure inside. In this process a pressure inside the dewar of about 400 mbar is reached, which corresponds to about 3.5 K [McC73].

6.2. Measurement and fitting process

For measuring a 2-port vector network analyzer (VNA) is used. For the theory on that see section 2.3. The practical part of measuring a resonator is simple. The interesting parameter is the S_{21} parameter of the scattering matrix, which describes the transmission
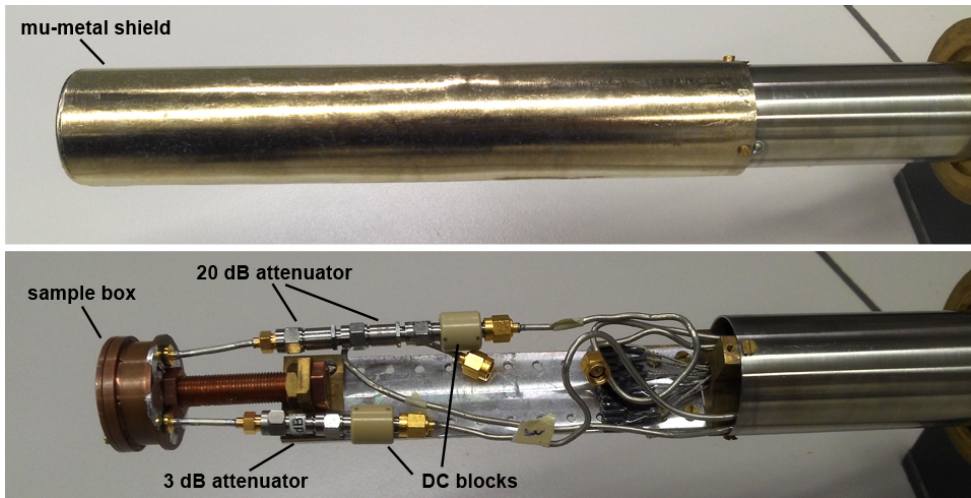
Figure 6.1 Dipstick with (top) and without (bottom) mu-metal shield. Only two of the four existing cables in the dipstick are used. The chip to be measured is in the sample box.

from port 1 to port 2. In between the two ports is the setup described in the previous section 6.1. When resonance occurs there is a dip in the transmission spectrum. In order to plot the phase properly the cable delay has to be substracted from the signal. This is done by the VNA when entering the length of the used cable. The more complicated part is the fitting of the measured data to get the resonance frequency and Q factor.

The fitting process of choice is called circle fit. When plotting the imaginary part of the transmission signal over the real part a circle is formed. This is shown in figure 6.2. A formula to describe and fit this circle is

$$\tilde{S}_{21}(f) = ae^{i\alpha}e^{-2\pi if\tau}\left(1 - \frac{Q_l}{|Q_c|}\cdot\frac{e^{i\Phi}}{1 + 2iQ_l(\frac{f-f_0}{f_0})}\right), \tag{6.1}$$

which is a slightly modified version of the formula used by J. Gao [Gao08]. Here a is a complex parameter accounting for amplification or attenuation in the setup, α is also a parameter to be fitted and τ is the signal delay caused by the length of the cable.
The magnitude of the fitted data is calculated by

$$|S_{21}| = 20 \cdot \log_{10}(|\tilde{S}_{21}|) \tag{6.2}$$

and the phase of the fitted data is the angle of the complex $\tilde{S}_{21}$.
Measurements showed that for a good fit of the resonance dip, the impedances before and after the dip should roughly match. If not, this is called impedance mismatch. If the impedance mismatch is too big the circle fit process hardly fits the dips slopes and sometimes not even the minimum is fitted correctly.

6.2.1. Circle fit

In this section we take a brief look at the mathematics behind the circle fit of both quadratures following the thesis of J. Gao [Gao08].
The circle is described by its center $z_c = x_c + iy_c$ and its radius r. To obtain this data a function
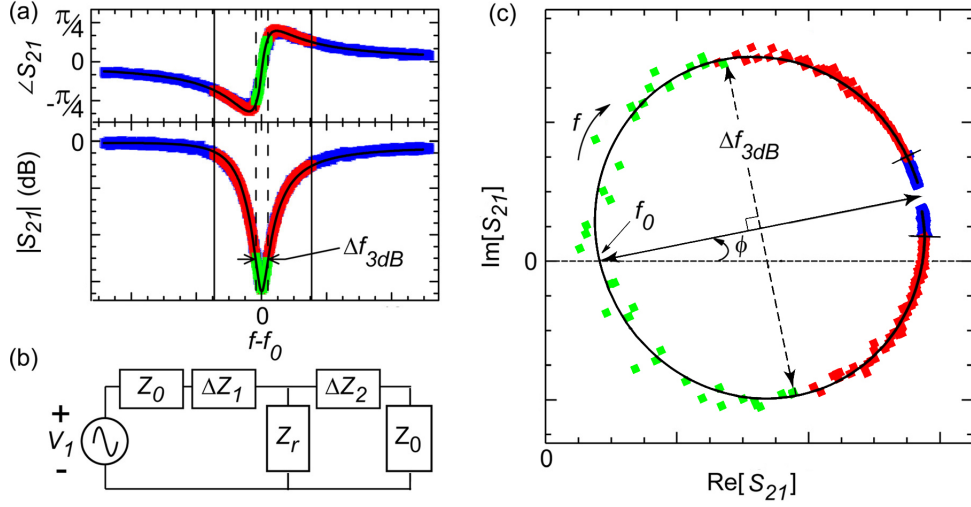
Figure 6.2 Sketch of circle fitting process. (a) shows the phase and magnitude of a S_{21} measurement, (b) shows the circuit diagram corresponding to the resonance frequency dip and (c) shows the circle that is formed when plotting the imaginary part of S_{21} over the real part of S_{21}. ΔZ_1 and ΔZ_2 in (b) are the complex impedances before and after the resonator, whereas Z_r and Z_0 belong to the resonator and the feedline. Figure after [MN⁺12].

$$\mathcal{F}(x_c, y_c, r) = \sum_{i=1}^{n} [Aw_i'^2 + Bx_i' + Cy_i' + D]^2, \tag{6.3}$$

which is restricted by $B^2 + C^2 - 4AD = 1$, must be minimized. Here $w_i'^2 = x_i'^2 + y_i'^2$. This can be written in matrix form $\mathcal{F} = A^T M A$, where the constraint can be written as $A^T B A = 1$.

$$A = (A, B, C, D)^T, \tag{6.4}$$

$$M = \begin{pmatrix} M_{ww} & M_{xw} & M_{yw} & M_w \\ M_{xw} & M_{xx} & M_{xy} & M_x \\ M_{yw} & M_{xy} & M_{yy} & M_y \\ M_w & M_x & M_y & n \end{pmatrix}, \quad B = \begin{pmatrix} 0 & 0 & 0 & -2 \\ 0 & 1 & 0 & 0 \\ 0 & 0 & 1 & 0 \\ -2 & 0 & 0 & 0 \end{pmatrix}, \tag{6.5}$$

where M_{ij} are the moments of the data, for example $M_{xw} = \sum_{i=1}^{n} = x_i w_i$. This problem can be solved by the Lagrange multiplier method. Here the multiplier η minimizes the function

$$\mathcal{F}_* = A^T M A - \eta(A^T B A - 1). \tag{6.6}$$

Differentiating with respects to A yields

$$MA - \eta BA = 0 \quad \rightarrow \quad \det(M - \eta B) = 0. \tag{6.7}$$

Solving this yields several η, where the smallest nonnegative η is the correct one [CL05]. With determined η the parameters A, B, C, D can be found resulting in the circle parameters

$$x_c = -\frac{B}{2A} \quad , y_c = -\frac{C}{2A} \quad , r = \frac{1}{4A^2}. \tag{6.8}$$

Further steps are the alignment to the real axis by the transformation

$$z_i'' = (z_c - z_i')e^{-i\alpha}, \tag{6.9}$$

where z_i' is the data to be fitted, z_c and $\alpha = \arg(z_c)$ are results of the fitting. The phase angle of z_i'' is obtained by

$$\theta = -\theta_0 + 2\tan^{-1}\left[2Q_l\left(1 - \frac{f}{f_0}\right)\right]. \tag{6.10}$$

At least the parameters Q_c and Φ can be found by

$$Q_c = \frac{|z_c| + r}{2r} \cdot Q_l \quad \text{and} \quad \Phi = \theta_0 - \arg(z_c). \tag{6.11}$$

To summarize, the circle fit yields a, f_0, Q_l, Q_c, α and Φ.
The internal quality factor Q_i is then defined by

$$\frac{1}{Q_i} = \frac{1}{Q_l} - \text{Re}\left\{\frac{1}{Q_c}e^{i\Phi}\right\} \tag{6.12}$$

6.3. Measurement and fitting results

In this section the measurements' results are discussed. Section 6.3.1 deals with first measurement and the several steps of improvements made on the setup. Since this measurement did not provide useful results due to limitations of the cryogenic setup, the second section 6.3.2 deals with the results of the reference measurement.

6.3.1. Measurement of manufactured chip and setup improvements

Figure 3.1 shows the design of the chip used for this measurement. This measurement is done to check whether the chip is working and the anodization process can be done. In the case that it is not working another chip has to be manufactured or taken for further experiments.

In this experiment two broad dips are expected, each consisting of 5 dips at the same frequency (see section 4.2). The first measuring process is done without the DC blocks in the setup (see section 6.1). This yields no results, since no dips are seen in the transmission spectrum. It is assumed that the copper cables in the dipstick warm up the chip since copper has a high heat conduction. Therefore the DC blocks are added into the setup. However, still no dips are seen in the spectrum.

In figure 6.3 the magnetic moment of the used Nb-film against temperature measured at a magnetic field of 50 Oe is shown. At the critical temperature the superconductor forms an internal magnetic moment against the external magnetic field to keep the superconductor field free. For the theory see section 2.1.2. Here the transition temperature is about 7.8 − 7.9 K, which is lower than the critical temperature of bulk Nb of 9.2 K. The reason for this might be an anisotropic growth of the Nb film and oxygen intake. Being too close to the critical temperature the resonator characteristics are suppressed. Since the critical temperature is lower than expected the used helium dewar is pumped to get to lower temperatures while measuring. In this process about 3.5 K are reached, but again there are no dips to be seen in the spectrum.

To get to even lower temperatures a different setup is necessary, which is more time-consuming and complicated. Due to the high volume of work associated with the new

setup it is not possible to complete it at this time. Therefore this experiment was stopped and a reference chip known to be working in this setup is measured (see next section 6.3.2). Although this experiment achieved no useful results, it at least shows that temperatures down to 3.5 K are too high for our 50 nm thick Nb resonators.
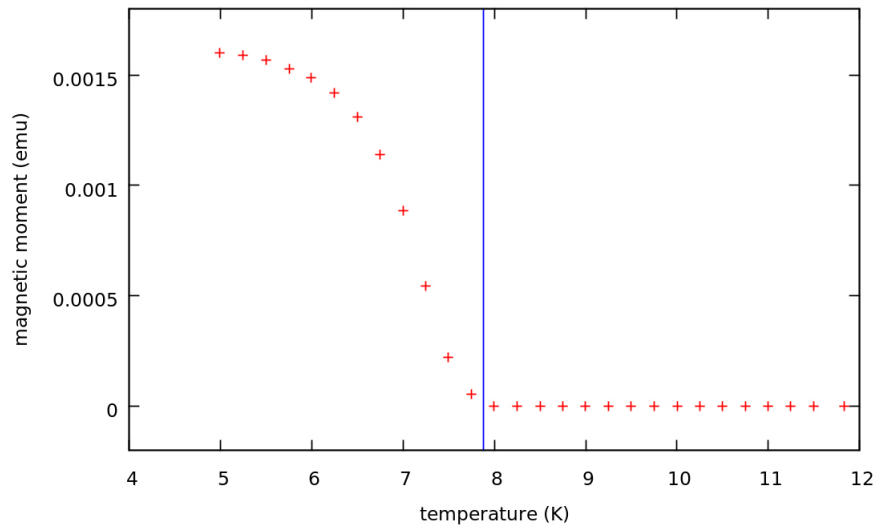

Figure 6.3 Magnetic moment of the Nb thin film against temperature measured at a magnetic field of 50 Oe. At about $7.8 - 7.9$ K the magnetic moment rises indicating T_c, thus the transition into superconductive state. The transition is marked by the blue line.

6.3.2. Reference chip measurement

In figure 6.4 the design of the chip used for this measurement is shown. This is an older chip known to be working in this setup and so it is used as a reference chip in this work. Since the actual chip did not work properly the reference chip is measured. There are seven resonators coupled to a feedline. The resonators all have the same coupling elements but are slightly different in length. The resonators are numbered from 1 to 7 for assigning to the results. From 1 to 7 the length of the resonators decreases, thus the resonance frequency increases. That can be seen in figure 6.5, where the transmission spectrum of the chip is plotted in the frequency range where all seven dips can be found.

This measurement is done without pumping on the helium dewar, thus at 4.2 K. The transmission S_{21} is measured and the results are fitted as explained in section 6.2. The plots for each measurement including fitted data can be found in appendix E. The results for resonance frequency and Q factors are listed in table 6.1.

The fit yields an error σ_{meas} that describes the fits quality in terms of deviation of the fitted points to the original points of the measurement. A higher σ_{meas} means less fit accuracy. For a $\sigma_{\mathrm{meas}} \approx 1 \cdot 10^{-5}$ the fitted and original curve can hardly be distinguished by eye, but results with a σ_{meas} of about 10^{-4} are still very good.

The results of dip 1 yield a high σ_{meas}, which is due to the known fact of the resonator coupling with the contact on the left side (see figure 6.4). This leads to a bad fit especially of the left slope in the magnitude. The fit of the slopes of dip 2 are also inaccurate but in both fits the minimum of the dip is still at the right position and therefore yields an useful value of the resonance frequency. The fitted data of the dips $3 - 6$ are much more accurate. Here the fitted and original curves are hardly distinguishable. The fit of dip 7 yields a shifted minimum, which also can be ascribed to the near contact on the right side of the chip.
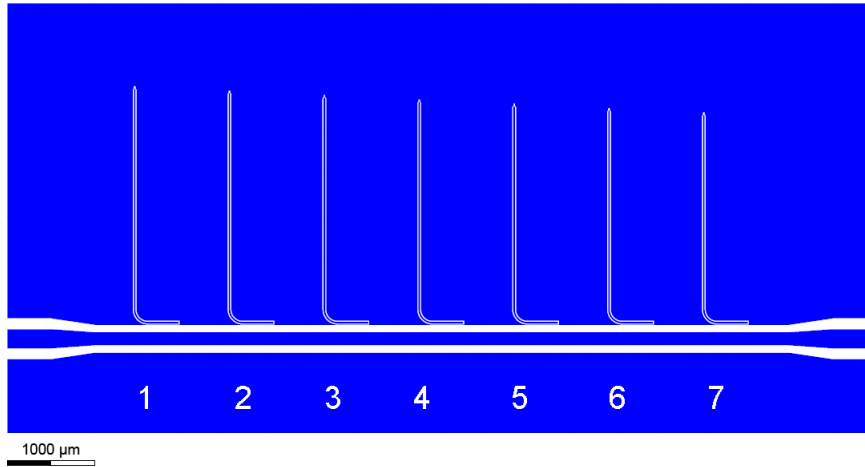
Figure 6.4 Overview of the design of the reference chip used in this work. Here seven resonators are coupled to the feedline. Their conductors width is 20 μm, the gap width is 11 μm and the thickness of the Nb film is 200 μm. The resonators are numbered from 1 to 7 to be assigned to the measurements results.

Table 6.1 Results of reference chip measurement and circle fitting process, resonance frequency, loaded Q factor, coupling and internal Q factor. The error σ_{meas} of the measurement represents the fitting quality in terms of deviation of the fitted points to the original points of the measurement. The smaller σ_{meas} the better is the fitted curve.

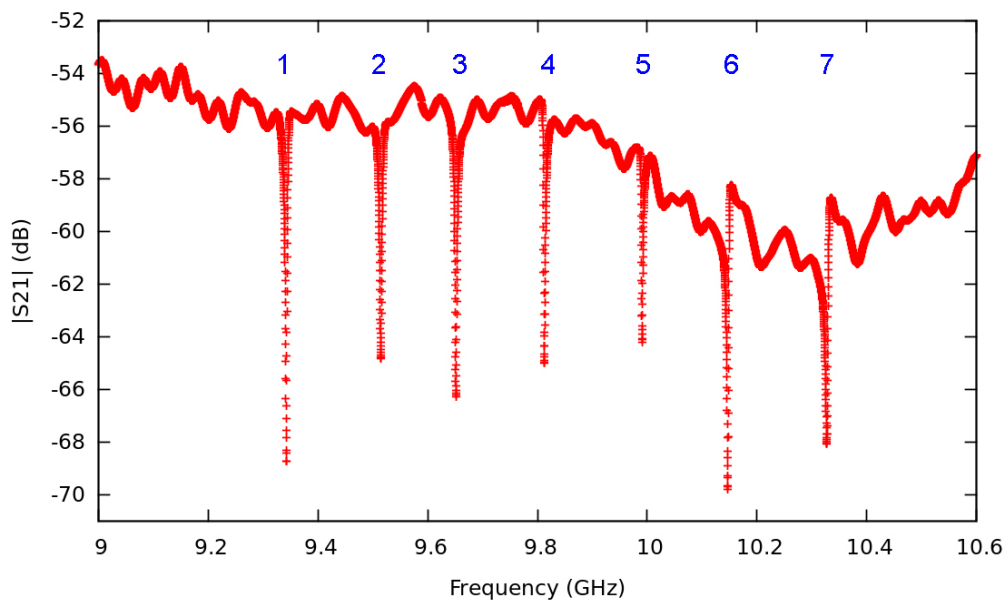| dip #	f_0 (GHz)	Q_{l} (10^3)	Q_{c} (10^3)	Q_{i} (10^3)	σ_{meas}
1	9.343	1.633	2.127	8.917	$5.797{\cdot}10^{-3}$
2	9.515	1.501	2.375	4.182	$2.771{\cdot}10^{-3}$
3	9.651	1.298	1.849	4.418	$4.525{\cdot}10^{-5}$
4	9.812	2.051	3.153	7.541	$7.652{\cdot}10^{-4}$
5	9.990	2.747	5.180	6.804	$2.417{\cdot}10^{-4}$
6	10.148	1.942	3.011	11.404	$1.701{\cdot}10^{-4}$
7	10.330	1.427	2.817	6.427	$2.433{\cdot}10^{-4}$

Figure 6.5 Transmission spectrum of reference chip showing all seven resonance dips. The numbering is the same as on the design in figure 6.4 and the listed results in table 6.1.

7. Conclusion

This thesis provides a diversified overview of the microwave resonator technology. In the theory part the most important knowledge of understanding the superconductive and resonant circuit properties of resonators is presented. Also the microwave network analysis, needed for measuring, and data interpretation is given.

The simulation section shows two different approaches of simulating microwave resonators. In particular the simulation with Sonnet gives a valuable insight into the electromagnetic properties using one of the major microwave circuit simulation softwares on the market.

For fabrication common technology of photolithography was used and is explained in the corresponding section of this thesis. The section on anodic oxidation might function as introduction to the application for further workings on this matter, even though it could not be used for this work.

Also the section on measuring might be taken as a basis for improving the setup and carrying on with the idea of this thesis. Starting points may be the improvement of the dipstick for a better thermal shielding or measurements at lower temperatures. If this works out the anodic oxidation process can be done and therefore the field distribution in superconducting microwave resonators can be studied experimentally.

Bibliography

[AM07]   N. W. Ashcroft and D. N. Mermin. *Festkörperphysik*. Oldenbourg, München, 2007.

[Bar09]   R. Barends. *Photon-detecting superconducting resonators*. PhD thesis, Technical University Delft, 2009.

[BTB87]   K. A. Blanks, A. E. Tabor, and K. Becker. Absolute cross sections for flourine 3p→3s line emissions following single electron impact on NF3, CF4, and SF6. *The Journal of Chemical Physics*, (86), 9 1987.

[CL05]   N. Chernov and C. Lesort. Least Squares Fitting of Circles. *Journal of Mathematical Imaging and Vision*, (23), 2005.

[Doy08]   S. Doyle. *Lumped Element Kinetic Inductance Detectors*. PhD thesis, Cardiff University, 2008.

[dS07]   A. I. Correia de Sá. *Anodic oxides on Al-Nb alloys and niobium*. PhD thesis, University of Mancheser, 2007.

[EH00]   C. Enss and S. Hunklinger. *Tieftemperaturphysik*. Springer, 2000.

[Eph81]   L. M. Ephrath. Reactive ion etching. Technical report, United States Patent, August 1981. Cross-reference to related applications.

[Gao08]   J. Gao. *The Physics of Superconducting Microwace Resonators*. PhD thesis, California Institut of Technology, Pasadina, California, 2008.

[Kai11]   C. Kaiser. *High Quality NB/Al-AlOx/Nb Josephson Junctions: Technological Development and Macroscopic Quantum Experiments*. PhD thesis, Karlsruher Institut für Technologie (KIT), 2011.

[Kit06]   Ch. Kittel. *Einführung in die Festkörperphysik*. Oldenbourg, München, 2006.

[KR12]   Dr. Ing. C. Koch and Dr. Ing. T. J. Rinke. Photolithography, 2012. Theory and Application of Photoresists, Etchants and Solvents.

[KSJ81]   H. Kroger, L. N. Smith, and D. W. Jillie. Selective niobium anodization process for fabricating Josephson tunnel junctions. *Applied Physics Letter*, 39(3), August 1981.

[Maz04]   B. A. Mazin. *Microwave Kinetic Inductance Detectors*. PhD thesis, California Institut of Technology, Pasadina, California, 2004.

[McC73]   R. D. McCarty. Thermodynamic Properties of Helium 4 from 2 to 1500 K at Pressures to 10^8 Pa. *J. Phys. Chem. Ref. Data*, 2(4), 1973.

[Mee10]   D. Meeker. *Finite Element Method Magnetics Version 4.2*. User's Manual, October 16, 2010. (http://www.femm.info).

[MN$^+$12] A. Megrant, C. Neill, et al. Planar superconducting resonators with internal quality factors above one million. *Applied Physics Letter*, 100(113510), 2012.

[Oeh86] G. S. Oehrlein. Reactive-ion etching. *Physics Today*, October 1986.

[Poz05] D. M. Pozar. *Microwave Engineering*. Wiley, 3 edition, 2005.

[Roh06] Rohm and Haas Electronic. *Microposit S 1800 G2 Series Photoresist*, October 2006.

[Sch97] V. V. Schmidt. *The Physics of Superconductors*. Springer, 1997.

[Shi] Shipley. *Microposit MF-319 Developer*.

[Son11] Sonnet Software Inc. *Sonnet User's Guide*, 13 edition, June 2011. (http://www.sonnetsoftware.com).

[Was03] R. Waser. *Nanoelectronics and Information Technology*. Wiley-VCH, 2003.

[Wei06] M. P. Weides. *Josephson tunnel junctions with ferromagnetic interlayer*. PhD thesis, Universität zu Köln, 2006.

Appendix

A. Lua-script for FEMM 4.2

```
clearconsole()
newdocument(1)

ei_probdef("micrometers","planar",1.E-8,(1),(30))



-- -- --VARIABLES

s=1 --"size in general"-parameter

w=s*10      --width of conductor
g=s*6 --width of gap
h=s*0.1 --height of conductor
sh=s*500   --height of substrat

e_vac=1 --relative permittivity of vacuum
e_sub=12 --relative permittivity of substrat
e_oxide=35 --relative permittivity of oxide

V_con=1 --voltage of conductor
V_gnd=0 --voltage of GND

ms=5 --mesh_size parameter

oudw=0 --width of oxide on top of metal and between metal and substrat
ow=0.15 --width of NbOx

ww=9*w+2*g  --entire width
MS=ms/s --meshsize dependand of meshsize parameter and "size in general"-parameter



--materials etc.

ei_deletematerial("MN_vacuum") --deletes materials if already exists
ei_deletematerial("MN_substrat")
ei_deletematerial("MN_NbOx")

ei_addmaterial("MN_vacuum", e_vac, e_vac, 0) --creates materials
ei_addmaterial("MN_substrat", e_sub, e_sub, 0)
ei_addmaterial("MN_NbOx", e_oxide, e_oxide, 0)

ei_addconductorprop("superconductor", V_con, 0, 1)
ei_addconductorprop("GND", V_gnd, 0, 1)
ei_addboundprop("ex_bound", 0, 0, 0, 0, 0)
```

```
-- -- --MODELL

--GND

ei_addnode(0,0)  --left
ei_addnode(0,h)
ei_addnode(4*w,0)
ei_addnode(4*w,h)

ei_addsegment(0,0,0,h)
ei_addsegment(0,0,4*w,0)
ei_addsegment(4*w,0,4*w,h)
ei_addsegment(0,h,4*w,h)

ei_addnode(5*w+2*g,0) --right
ei_addnode(5*w+2*g,h)
ei_addnode(9*w+2*g,0)
ei_addnode(9*w+2*g,h)

ei_addsegment(5*w+2*g,0,5*w+2*g,h)
ei_addsegment(5*w+2*g,0,ww,0)
ei_addsegment(5*w+2*g,h,ww,h)
ei_addsegment(ww,0,ww,h)

ei_selectsegment(0,h/2) --set properties
ei_selectsegment(2*w,0)
ei_selectsegment(4*w,h/2)
ei_selectsegment(2*w,h)
ei_selectsegment(5*w+2*g,h/2)
ei_selectsegment(ww-w,0)
ei_selectsegment(ww,h/2)
ei_selectsegment(ww-w,h)

ei_setsegmentprop("", 0, 1, 0, 2, "GND")

ei_clearselected()

ei_addblocklabel(2*w,h/2) --label
ei_addblocklabel(7*w+2*g,h/2)
ei_selectlabel(2*w,h/2)
ei_selectlabel(7*w+2*g,h/2)

ei_setblockprop("<No Mesh>", 1, 0, 0)

ei_clearselected()


if oudw > 0 then

ei_addnode(0,h-oudw) --left
ei_addnode(4*w,h-oudw)
ei_addnode(0,oudw)
ei_addnode(4*w,oudw)

ei_addsegment(0,h-oudw,4*w,h-oudw)
ei_addsegment(0,oudw,4*w,oudw)
```

```
ei_addblocklabel(2*w,h-oudw/2)
ei_addblocklabel(2*w,oudw/2)




ei_addnode(5*w+2*g,h-oudw) --right
ei_addnode(ww,h-oudw)
ei_addnode(5*w+2*g,oudw)
ei_addnode(ww,oudw)

ei_addsegment(5*w+2*g,h-oudw,ww,h-oudw)
ei_addsegment(5*w+2*g,oudw,ww,oudw)

ei_addblocklabel(ww-2*w,h-oudw/2)
ei_addblocklabel(ww-2*w,oudw/2)

end


--conductor

ei_addnode(4*w+g,0)
ei_addnode(4*w+g,h)
ei_addnode(5*w+g,0)
ei_addnode(5*w+g,h)

ei_addsegment(4*w+g,0,4*w+g,h)
ei_addsegment(4*w+g,h,5*w+g,h)
ei_addsegment(5*w+g,h,5*w+g,0)
ei_addsegment(5*w+g,0,4*w+g,0)


ei_selectsegment(4*w+g,h/2) --set properties
ei_selectsegment(5*w+g,h/2)
ei_selectsegment(4.5*w+g,h)
ei_selectsegment(4.5*w+g,0)

ei_setsegmentprop("", 0, 1, 0, 1, "superconductor")

ei_clearselected()

ei_addblocklabel(4.5*w+g,h/2) --label
ei_selectlabel(4.5*w+g,h/2)

ei_setblockprop("<No Mesh>", 1, 0, 0)

ei_clearselected()

--oxide on top of metal and between metal and substrat
if oudw > 0 then

ei_addnode(4*w+g,h-oudw)
ei_addnode(5*w+g,h-oudw)
ei_addnode(4*w+g,oudw)
ei_addnode(5*w+g,oudw)

ei_addsegment(4*w+g,h-oudw,5*w+g,h-oudw)
ei_addsegment(4*w+g,oudw,5*w+g,oudw)
```

```
ei_addblocklabel(4.5*w+g,h-oudw/2)
ei_addblocklabel(4.5*w+g,oudw/2)

end


--gap

ei_addsegment(4*w,0,4*w+g,0)
ei_addsegment(5*w+g,0,5*w+2*g,0)
ei_addsegment(4*w,h,4*w+g,h)
ei_addsegment(5*w+g,h,5*w+2*g,h)

ei_addblocklabel(4*w+g/2,h/2) --blocklabel
ei_addblocklabel(5*w+1.5*g,h/2)
ei_selectlabel(4*w+g/2,h/2)
ei_selectlabel(5*w+1.5*g,h/2)

ei_setblockprop("MN_vacuum", 0, MS*0.01, 0)

ei_clearselected()


--substrat

ei_addnode(0,-sh)
ei_addnode(ww,-sh)

ei_addnode(0,-sh/5)
ei_addnode(ww,-sh/5)

ei_addnode(0,-sh/10)
ei_addnode(ww,-sh/10)

ei_addnode(0,-2.5*w)
ei_addnode(ww,-2.5*w)

ei_addsegment(0,0,0,-sh)
ei_addsegment(ww,0,ww,-sh)
ei_addsegment(0,-sh/5,ww,-sh/5)
ei_addsegment(0,-sh/10,ww,-sh/10)
ei_addsegment(0,-sh,ww,-sh)
ei_addsegment(0,-2.5*w,ww,-2.5*w)

ei_addnode(2.5*w,0)  --little box in the middle
ei_addnode(2.5*w,-w)
ei_addnode(6.5*w+2*g,-w)
ei_addnode(6.5*w+2*g,0)

ei_addsegment(2.5*w,0,2.5*w,-w)
ei_addsegment(2.5*w,-w,6.5*w+2*g,-w)
ei_addsegment(6.5*w+2*g,-w,6.5*w+2*g,0)

ei_addblocklabel(ww/2,-w/2) --blocklabels and mesh
ei_selectlabel(ww/2,-w/2)
ei_setblockprop("MN_substrat", 0, MS*0.02, 0)
ei_clearselected()

ei_addblocklabel(ww/2,-1.5*w)
```

```
ei_selectlabel(ww/2,-1.5*w)
ei_setblockprop("MN_substrat", 0, MS*0.15, 0)
ei_clearselected()

ei_addblocklabel(ww/2,-sh/11)
ei_selectlabel(ww/2,-sh/11)
ei_setblockprop("MN_substrat", 0, MS*1, 0)
ei_clearselected()

ei_addblocklabel(ww/2,-sh/7)
ei_selectlabel(ww/2,-sh/7)
ei_setblockprop("MN_substrat", 0, MS*5, 0)
ei_clearselected()

ei_addblocklabel(ww/2,-sh/2)
ei_selectlabel(ww/2,-sh/2)
ei_setblockprop("MN_substrat", 0, MS*20, 0)
ei_clearselected()


--vacuum

ei_addnode(2.5*w,h)  --little box in the middle
ei_addnode(2.5*w,w+h)
ei_addnode(6.5*w+2*g,w+h)
ei_addnode(6.5*w+2*g,h)

ei_addsegment(2.5*w,h,2.5*w,w+h)
ei_addsegment(2.5*w,w+h,6.5*w+2*g,w+h)
ei_addsegment(6.5*w+2*g,w+h,6.5*w+2*g,h)

ei_addblocklabel(ww/2,h+w/2)
ei_selectlabel(ww/2,h+w/2)
ei_setblockprop("MN_vacuum", 0, MS*0.02, 0)
ei_clearselected()


ei_addnode(0,h+2.5*w) --bigger little box
ei_addnode(ww,h+2.5*w)

ei_addsegment(0,h,0,h+2.5*w)
ei_addsegment(0,h+2.5*w,ww,h+2.5*w)
ei_addsegment(ww,h,ww,h+2.5*w)

ei_addblocklabel(ww/2,h+1.5*w)
ei_selectlabel(ww/2,h+1.5*w)
ei_setblockprop("MN_vacuum", 0, MS*0.15, 0)
ei_clearselected()


ei_addnode(-sh/10,0) --smaller box inside
ei_addnode(ww+sh/10,0)
ei_addnode(0,h+sh/10)
ei_addnode(ww,h+sh/10)

ei_addsegment(0,-sh/10,-sh/10,0)
ei_addsegment(-sh/10,0,0,h+sh/10)
ei_addsegment(0,h+sh/10,ww,h+sh/10)
ei_addsegment(ww,h+sh/10,ww+sh/10,0)
```

```
ei_addsegment(ww+sh/10,0,ww,-sh/10)

ei_addblocklabel(ww/2,h+sh/11)
ei_selectlabel(ww/2,h+sh/11)
ei_setblockprop("MN_vacuum", 0, MS*1, 0)
ei_clearselected()


ei_addnode(-sh/5,0) --bigger box inside
ei_addnode(ww+sh/5,0)
ei_addnode(0,h+sh/5)
ei_addnode(ww,h+sh/5)

ei_addsegment(0,-sh/5,-sh/5,0)
ei_addsegment(-sh/5,0,0,h+sh/5)
ei_addsegment(0,h+sh/5,ww,h+sh/5)
ei_addsegment(ww,h+sh/5,ww+sh/5,0)
ei_addsegment(ww+sh/5,0,ww,-sh/5)

ei_addblocklabel(ww/2,h+sh/7)
ei_selectlabel(ww/2,h+sh/7)
ei_setblockprop("MN_vacuum", 0, MS*5, 0)
ei_clearselected()


ei_addnode(-sh,0) --exterior border
ei_addnode(sh+ww,0)
ei_addnode(-sh/2,2*sh/3)
ei_addnode(sh/2+ww,2*sh/3)

ei_addsegment(-sh,0,0,-sh)
ei_addsegment(ww,-sh,sh+ww,0)
ei_addsegment(-sh,0,-sh/2,2*sh/3)
ei_addsegment(-sh/2,2*sh/3,sh/2+ww,2*sh/3)
ei_addsegment(sh/2+ww,2*sh/3,sh+ww,0)

ei_addblocklabel(ww/2,h+sh/2)
ei_selectlabel(ww/2,h+sh/2)
ei_setblockprop("MN_vacuum", 0, MS*20, 0)
ei_clearselected()


ei_selectsegment(-sh/2,-sh/2) --set boundary condition
ei_selectsegment(ww+sh/2,-sh/2)
ei_selectsegment(-3*sh/4,sh/3)
ei_selectsegment(0,2*sh/3)
ei_selectsegment(ww+3*sh/4,sh/3)

ei_setsegmentprop("ex_bound", 0, 1, 0, 3, "")

ei_clearselected()


--OXIDE

if ow > 0 then

ei_addnode(4*w+ow,0)
ei_addnode(4*w+ow,h)
```

```
ei_addnode(4*w+g-ow,0)
ei_addnode(4*w+g-ow,h)
ei_addnode(5*w+g+ow,0)
ei_addnode(5*w+g+ow,h)
ei_addnode(5*w+2*g-ow,0)
ei_addnode(5*w+2*g-ow,h)

ei_addsegment(4*w+ow,0,4*w+ow,h)
ei_addsegment(4*w+g-ow,0,4*w+g-ow,h)
ei_addsegment(5*w+g+ow,0,5*w+g+ow,h)
ei_addsegment(5*w+2*g-ow,0,5*w+2*g-ow,h)

ei_addblocklabel(4*w+ow/2,h/2)
ei_addblocklabel(4*w+g-ow/2,h/2)
ei_addblocklabel(5*w+g+ow/2,h/2)
ei_addblocklabel(5*w+2*g-ow/2,h/2)

ei_selectlabel(4*w+ow/2,h/2)
ei_selectlabel(4*w+g-ow/2,h/2)
ei_selectlabel(5*w+g+ow/2,h/2)
ei_selectlabel(5*w+2*g-ow/2,h/2)

ei_setblockprop("MN_NbOx", 0, MS*0.01, 0)

ei_clearselected()

end


-- -- --other things

--zooming

ei_zoom(11,-10,40,8)


--save, create mesh and analyze problem


ei_saveas("test.fee")
ei_createmesh()
ei_analyze(1)
ei_loadsolution()
```

B. Calculations

B.1. Geometric capacitance and inductance of 10/6 CPW resonator

(see 2.2.5.1)

$$\epsilon_{\mathrm{r}} = 12 \tag{7.1}$$

$$w = 10\mu m \tag{7.2}$$

$$g = 6\mu m \tag{7.3}$$

$$\rightarrow k = \frac{w}{w + 2g} = 0,455 \tag{7.4}$$

$$k' = \sqrt{1 - k^2} = 0,891 \tag{7.5}$$

Using

$$K = K(k) = \int_0^1 \frac{1}{\sqrt{(1 - x^2)(1 - k^2 x^2)}} \, dx \tag{7.6}$$

$$K' = K(k') = \int_1^{1/k} \frac{1}{\sqrt{(x^2 - 1)(1 - k^2 x^2)}} \, dx \tag{7.7}$$

leads to

$$K = 1,663 \tag{7.8}$$

$$K' = 2,242 \tag{7.9}$$

$$\epsilon_{\mathrm{eff}} = \frac{1 + \epsilon_{\mathrm{r}}}{2} = 6,5 \tag{7.10}$$

$$\Rightarrow C_{\mathrm{eff}} = 1,707 \cdot 10^{-16} \, \frac{F}{\mu m} \tag{7.11}$$

$$\Rightarrow L_{\mathrm{eff}} = 0,424 \cdot 10^{-13} \, \frac{H}{\mu m} \tag{7.12}$$

C. Simulation data

C.1. FEMM simulation results

Table C.1 Specific stored energy, specific capacitance and resonance frequency of CPW resonator for oxide layer with thickness t_{oxide} formed only in the gap without decreasing Nb layer thickness.

t_{oxide} (nm)	E (J/μm)	C (F/μm)	f$_0$ (GHz)
0	$8.50091 \cdot 10^{-17}$	$1.70018 \cdot 10^{-16}$	8.01329
25	$8.51650 \cdot 10^{-17}$	$1.70330 \cdot 10^{-16}$	8.00596
50	$8.54377 \cdot 10^{-17}$	$1.70875 \cdot 10^{-16}$	7.99317
75	$8.56381 \cdot 10^{-17}$	$1.71276 \cdot 10^{-16}$	7.98381
100	$8.58261 \cdot 10^{-17}$	$1.71652 \cdot 10^{-16}$	7.97506
125	$8.60504 \cdot 10^{-17}$	$1.72101 \cdot 10^{-16}$	7.96466
150	$8.62046 \cdot 10^{-17}$	$1.72409 \cdot 10^{-16}$	7.95754

Table C.2 Stored energy in the different materials of the CPW resonator with oxide layer on top of the Nb of thickness t. The different values for energy correspond to the energy stored in their respective meterials. Here tot = total system, vac = vacuum, sub = substrate and ox = oxide layer

t_{NbO_x} (nm)	t_{Nb} (nm)	E_{tot} (J/μm)	E_{vac} (J/μm)	E_{sub} (J/μm)	E_{ox} (J/μm)
0	50.00	$8.48 \cdot 10^{-17}$	$6.85 \cdot 10^{-18}$	$7.80 \cdot 10^{-17}$	0
25	40.22	$8.51 \cdot 10^{-17}$	$6.89 \cdot 10^{-18}$	$7.81 \cdot 10^{-17}$	$7.96 \cdot 10^{-20}$
50	30.43	$8.53 \cdot 10^{-17}$	$6.94 \cdot 10^{-18}$	$7.82 \cdot 10^{-17}$	$1.47 \cdot 10^{-19}$
75	20.65	$8.55 \cdot 10^{-17}$	$6.98 \cdot 10^{-18}$	$7.83 \cdot 10^{-17}$	$2.23 \cdot 10^{-19}$
100	10.87	$8.57 \cdot 10^{-17}$	$7.00 \cdot 10^{-18}$	$7.84 \cdot 10^{-17}$	$3.23 \cdot 10^{-19}$
125	1.09	$8.54 \cdot 10^{-17}$	$7.02 \cdot 10^{-18}$	$7.84 \cdot 10^{-17}$	$5.19 \cdot 10^{-19}$

Table C.3 Specific capacitances c for the various layers of the resonator system for increasing oxide layer thickness and decreasing Nb layer thickness. Here tot stands for total, vac stands for vacuum, sub stands for substrate and ox stands for oxide layer.

t_{NbO_x} (nm)	t_{Nb} (nm)	c_{tot} (F/μm)	c_{vac} (F/μm)	c_{sub} (F/μm)	c_{ox} (F/μm)
0	50.00	$1{,}70 \cdot 10^{-16}$	$1{,}37 \cdot 10^{-17}$	$1{,}56 \cdot 10^{-16}$	-
25	40.22	$1{,}70 \cdot 10^{-16}$	$1{,}38 \cdot 10^{-17}$	$1{,}56 \cdot 10^{-16}$	$1{,}59 \cdot 10^{-19}$
50	30.43	$1{,}71 \cdot 10^{-16}$	$1{,}39 \cdot 10^{-17}$	$1{,}56 \cdot 10^{-16}$	$2{,}93 \cdot 10^{-19}$
75	20.65	$1{,}71 \cdot 10^{-16}$	$1{,}40 \cdot 10^{-17}$	$1{,}57 \cdot 10^{-16}$	$4{,}47 \cdot 10^{-19}$
100	10.87	$1{,}71 \cdot 10^{-16}$	$1{,}40 \cdot 10^{-17}$	$1{,}57 \cdot 10^{-16}$	$6{,}46 \cdot 10^{-19}$
125	1.09	$1{,}71 \cdot 10^{-16}$	$1{,}40 \cdot 10^{-17}$	$1{,}57 \cdot 10^{-16}$	$1{,}04 \cdot 10^{-18}$

Table C.4 Inductivity L of the resonator system for increasing oxide layer thickness and decreasing Nb layer thickness. Here tot stands for total, int stands for intern, ext stands for extern and ana stands for analytical.

t_{NbO_x} (nm)	t_{Nb} (nm)	L_{int} (H/μm)	L_{int} (H/sq)	L_{int} (H)	$L_{\text{ext,ana}}$ (H)	L_{tot} (H)
0	50.00	$2{,}09{\cdot}10^{-14}$	$2{,}09{\cdot}10^{-13}$	$3{,}07{\cdot}10^{-10}$	$6{,}23{\cdot}10^{-09}$	$6{,}54{\cdot}10^{-09}$
25	40.22	$2{,}57{\cdot}10^{-14}$	$2{,}57{\cdot}10^{-13}$	$3{,}78{\cdot}10^{-10}$	$6{,}23{\cdot}10^{-09}$	$6{,}61{\cdot}10^{-09}$
50	30.43	$3{,}38{\cdot}10^{-14}$	$3{,}38{\cdot}10^{-13}$	$4{,}96{\cdot}10^{-10}$	$6{,}23{\cdot}10^{-09}$	$6{,}73{\cdot}10^{-09}$
75	20.65	$4{,}95{\cdot}10^{-14}$	$4{,}95{\cdot}10^{-13}$	$7{,}28{\cdot}10^{-10}$	$6{,}23{\cdot}10^{-09}$	$6{,}96{\cdot}10^{-09}$
100	10.87	$9{,}38{\cdot}10^{-14}$	$9{,}38{\cdot}10^{-13}$	$1{,}38{\cdot}10^{-09}$	$6{,}23{\cdot}10^{-09}$	$7{,}61{\cdot}10^{-09}$
125	1.09	$9{,}36{\cdot}10^{-13}$	$9{,}36{\cdot}10^{-12}$	$1{,}38{\cdot}10^{-08}$	$6{,}23{\cdot}10^{-09}$	$2{,}00{\cdot}10^{-08}$

Table C.5 Resonance frequency, loss and Q-factor the resonator system for increasing oxide layer thickness and decreasing Nb layer thickness. Here i stands for intern.

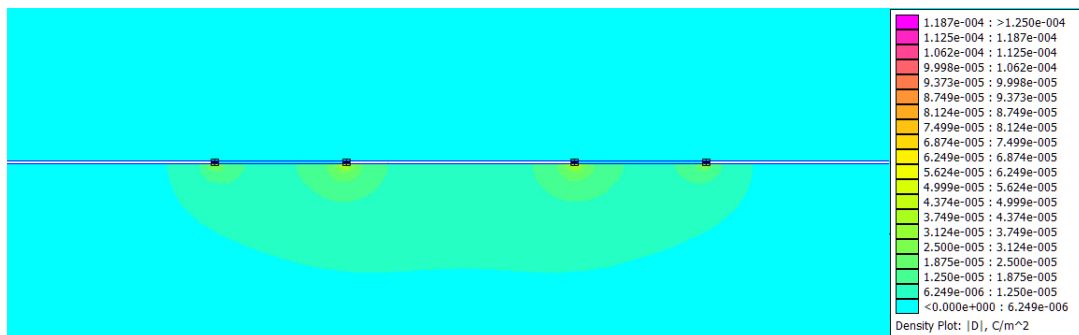| t_{NbO_x} (nm)	t_{Nb} (nm)	f_0 (Hz)	d_{i}	Q_{i}
0	50.00	$7{,}83{\cdot}10^9$	$1{,}00{\cdot}10^{-06}$	$1{,}00{\cdot}10^6$
25	40.22	$7{,}78{\cdot}10^9$	$1{,}93{\cdot}10^{-06}$	$5{,}17{\cdot}10^5$
50	30.43	$7{,}70{\cdot}10^9$	$2{,}72{\cdot}10^{-06}$	$3{,}68{\cdot}10^5$
75	20.65	$7{,}56{\cdot}10^9$	$3{,}61{\cdot}10^{-06}$	$2{,}77{\cdot}10^5$
100	10.87	$7{,}22{\cdot}10^9$	$4{,}76{\cdot}10^{-06}$	$2{,}10{\cdot}10^5$
125	1.09	$4{,}46{\cdot}10^9$	$7{,}08{\cdot}10^{-06}$	$1{,}41{\cdot}10^5$

Figure C.1 Flux density plot of the CPW resonator's cross section created with FEMM. Here the oxide layer is formed only in the gap next to the edge of the Nb film.

D. Fabrication data

Spin coating, optical resist

- resist S1805 G2 from micro resist technology

- cover at least 60% surface with resist before spinning

- 500rpm for 10 sec and 4500 rpm for 90 sec

- Ramp rate: 500rpm/sec

- 115°C hotbake on Cu plate for 60sec

- exposure

- Developing: MF-319 for 1 min, Isopropanol for a few min, DD water for a few min

Spin coating for sawing

- put thick protective layer on chip

- resist S1805 G2 from micro resist technology

- cover at least 60% surface with resist before spinning

- 500rpm for 10 sec and 1000 rpm for 90 sec

- Ramp rate: 500rpm/sec

- 90°C hotbake on Cu plate for 60sec

Notice that the recipe for sawing is also used for fabrication process in this work. This also leads to very good results as no sub-micron features are used.

Resist Stripper
Carl Roth (http://www.carlroth.com)

- DMF:
  N,N-Dimethylformamid (C_3H_7NO)
  disposal into separate, individual waste bottle

- NMP:
  N-Methyl-2-pyrrolidon (C_5H_9NO)
  or N-Ethyl-2-pyrrolidon ($C_6H_{11}NO$)
  disposal into halogene-free waste bottle

Put the sample in the stripper for several minutes, then put it in H_2O or Isopropanol for several minutes to wash the stripper off the sample.

Maskaligning specifications

- SUSS MA6 mask aligner

- hard contact mode

- lamp power: 350 W

- Intensity: 5 $\frac{mW}{cm^2}$

- duration of exposure: 4.5 s

SF6 RIE

- temperature of electrode: 23°C

- high vacuum

- gas flow: MFC2 11 sccm SF_6

- reactor pressure: 14 Pa

- HF-Generator power: 50 W

- duration of etching: 8 min

Anodic Oxidation

- electrolyte:
  156 g ammonium pentaborate
  1120 ml ethylene glycol
  760 ml H_2O

- 1V $\approx$ 0.9 nm consumed Nb and 2.3 nm formed NbO_x

E. Measurement results

Here the plots of the measurement (see section 6.3.2) are shown. The plots are arranged in the same order as on the chip (see figure 6.4) and are numbered from 1 to 7. Each first plot is the circle plot including fitted data, each second plot is the magnitude of the transmission measurement including the fitted data and each third plot is the phase of the measurement including fitted data.
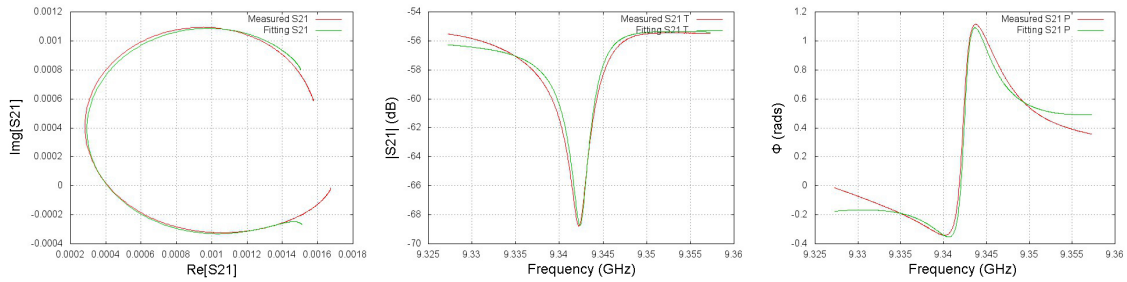

Figure E.2 Circle plot including fitted data (left), magnitude plot including fitted data (middle) and phase plot including fitted data of dip 1.
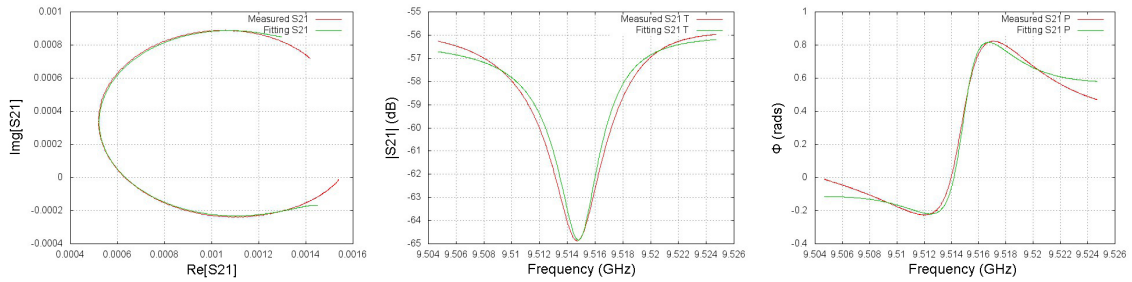
Figure E.3 Circle plot including fitted data (left), magnitude plot including fitted data (middle) and phase plot including fitted data of dip 2.
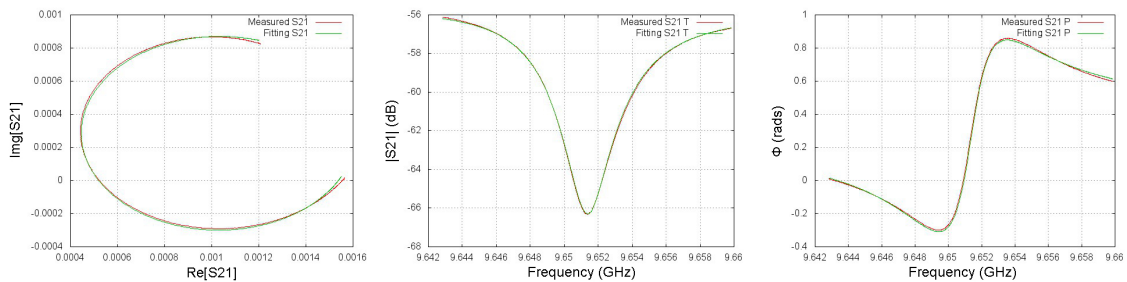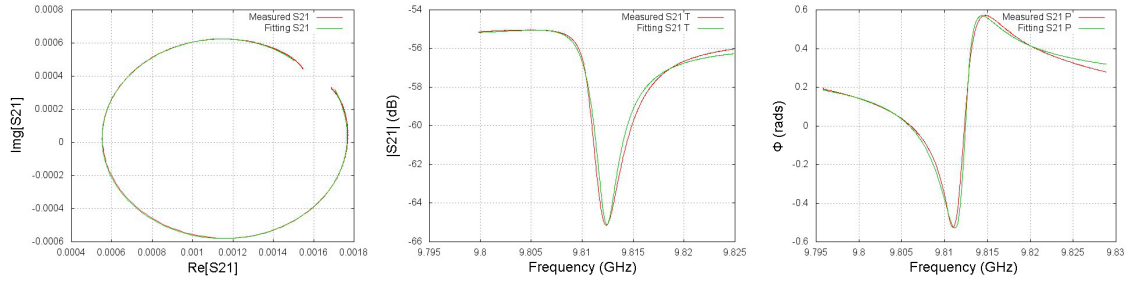

Figure E.4 Circle plot including fitted data (left), magnitude plot including fitted data (middle) and phase plot including fitted data of dip 3.

Figure E.5 Circle plot including fitted data (left), magnitude plot including fitted data (middle) and phase plot including fitted data of dip 4.
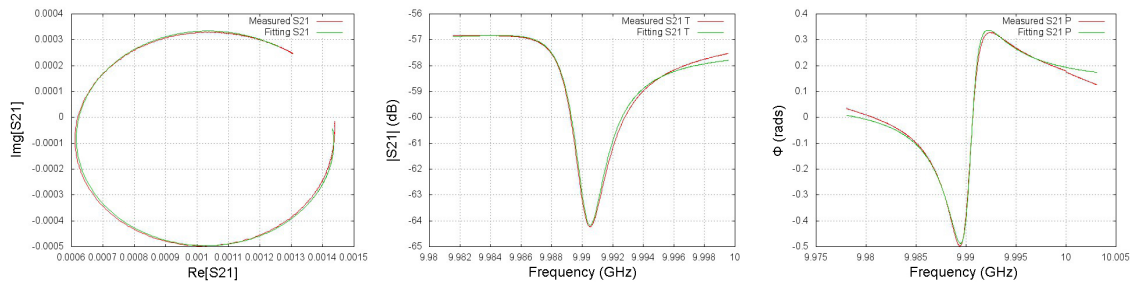

Figure E.6 Circle plot including fitted data (left), magnitude plot including fitted data (middle) and phase plot including fitted data of dip 5.
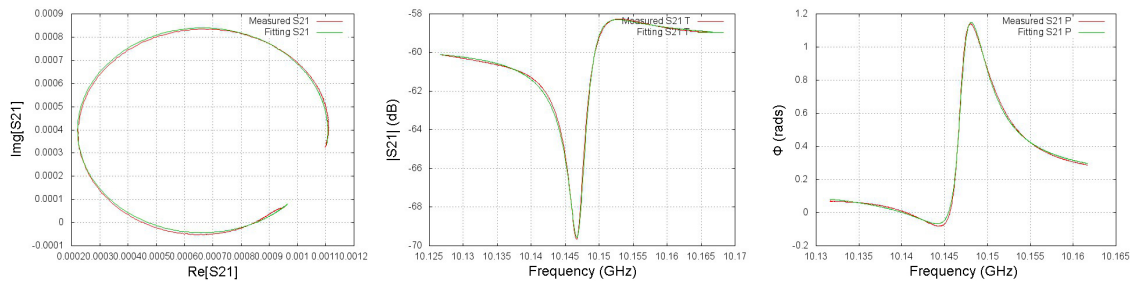

Figure E.7 Circle plot including fitted data (left), magnitude plot including fitted data (middle) and phase plot including fitted data of dip 6.
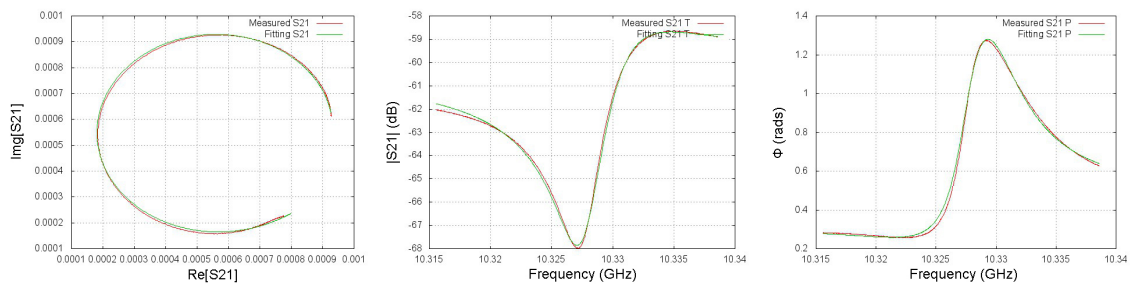

Figure E.8 Circle plot including fitted data (left), magnitude plot including fitted data (middle) and phase plot including fitted data of dip 7.

Acknowledgment

Not only during the progress of this work but during the last years of study I was supported by many people. Therefore I would like to state a few words of thanks.

Prof. Dr. Alexey Ustinov
I would like to thank you for the opportunity of doing my thesis in your research group.

Dr. Martin Weides
I want to thank you for this wide-ranging work, which gave me great insight into many aspects of your research. Although some parts of this work were lengthened I always had fun working with you on this matter.

Group Ustinov
I would like to thank all members of the research group for helping me in times of need. Especially Philipp Mayer and Lucas Radtke for helping me with cleanroom applications, and Dr. Fengbin Song for helping me with the measurement setup and computer problems. Furthermore I'd like to thank Susanne Butz, Philipp Jung, Sebastian Probst and finally Dr. Gerda Fischer for the SQUID data and Dr. Hannes Rotzinger for beeing second advisor.

Prof. Dr. Gernot Goll
I would like to thank you for the opportunity of working in the CFN cleanroom.

Friends
I would like to thank Joel Cramer, Johannes Fischer, Johannes King, Daniel Schell and Justus Zorn for being there for me during the last years. Without you I wouldn't be were I am right now.

Family
I would like to thank my family for being there for me all the time and support me in going my way.

Isabel
Last but not least I want to thank my girlfriend Isabel for being the best.